



UPPSALA  
UNIVERSITET

*Digital Comprehensive Summaries of Uppsala Dissertations  
from the Faculty of Science and Technology 871*

# First Principle Studies of Functional Materials

*Spintronics, Hydrogen Storage and Cutting Tools*

FREDRIK SILVEARV



ACTA  
UNIVERSITATIS  
UPSALIENSIS  
UPPSALA  
2011

ISSN 1651-6214  
ISBN 978-91-554-8191-9  
urn:nbn:se:uu:diva-160270

Dissertation presented at Uppsala University to be publicly examined in Siegbahnsalen, Ångström Laboratory, Lägerhyddsvägen 1, Uppsala. Friday, December 2, 2011 at 13:00 for the degree of Doctor of Philosophy. The examination will be conducted in English.

#### **Abstract**

Silvearv, F. 2011. First Principle Studies of Functional Materials: Spintronics, Hydrogen Storage and Cutting Tools. Acta Universitatis Upsaliensis. *Digital Comprehensive Summaries of Uppsala Dissertations from the Faculty of Science and Technology* 871. 60 pp. Uppsala. ISBN 978-91-554-8191-9.

The properties of functional materials have been studied with density functional theory.

The first type of materials that have been investigated is the so called diluted magnetic semiconductors. It is a new class of materials that could offer enhanced functionality by making use of spin in addition to the charge of the electron. (Mn,Al) co-doped ZnO has been investigated regarding the Al significance on ferromagnetic behavior using density functional theory within the generalized-gradient approximation plus on-site Coulomb interaction. Despite the presence of Al the system always shows antiferromagnetic behavior. The role of intrinsic defects on ferromagnetism in pure and Cr doped  $\text{In}_2\text{O}_3$  was also studied. For pristine  $\text{In}_2\text{O}_3$ , In vacancy and O interstitial states are completely spin polarized. Moreover, these hole states will create Cr ions in mixed valence state, giving rise to a strong ferromagnetic coupling.

The second type of functional materials studied are hydrogen storage materials for mobile applications. These materials are considered as alternative if hydrogen is to replace fossil fuels as a energy carrier. In the view of this a series of compounds containing boron, nitrogen and hydrogen has been examined with respect to electronic structure, dehydrogenation energy and hydrogen diffusion properties. One compound,  $\text{NH}_3\text{BH}_3$ , has many desirable properties as a hydrogen storage material. In an effort to improve those properties, one of the H atoms in the  $\text{NH}_3$  group was replaced by Li, Na or Sr. The calculated hydrogen removal energies of the hydrogen release reactions were found to be significantly improved.

Finally, a coating material,  $\text{Al}_2\text{O}_3$ , for wear resistant coatings on high performance cemented carbide cutting tools has been investigated. Chemical vapor deposition grown  $\text{Al}_2\text{O}_3$  has been used for decades by the industry. To improve the growth process  $\text{H}_2\text{S}$  is added to the gas mixture. The catalytic effect of  $\text{H}_2\text{S}$  on the  $\text{AlCl}_3/\text{H}_2/\text{CO}_2/\text{HCl}$  chemical vapor deposition process has been investigated on an atomistic scale. By applying a combined approach of thermodynamic modeling and density functional theory it seems that  $\text{H}_2\text{S}$  acts as mediator for the oxygenation of the Al-surface which will in turn increase the growth rate of  $\text{Al}_2\text{O}_3$ .

*Keywords:* spintronics, hydrogen storage, coating materials

*Fredrik Silvearv, Uppsala University, Department of Physics and Astronomy, Materials Theory, Box 516, SE-751 20 Uppsala, Sweden.*

© Fredrik Silvearv 2011

ISSN 1651-6214

ISBN 978-91-554-8191-9

urn:nbn:se:uu:diva-160270 (<http://urn.kb.se/resolve?urn=urn:nbn:se:uu:diva-160270>)

*Reality is God's Dream*



# List of papers

This thesis is based on the following papers, which are referred to in the text by their Roman numerals.

- I *Defect-induced strong ferromagnetism in Cr-doped  $\text{In}_2\text{O}_3$  from first-principles theory*  
L. M. Huang, F. Silvearv, C. Moysés Araújo and R. Ahuja  
Solid State Communications **150**, 663 (2009).
- II *Structural and energetic analysis of the hydrogen storage materials  $\text{LiNH}_2\text{BH}_3$  and  $\text{NaNH}_2\text{BH}_3$  from ab initio calculations*  
M. Ramzan, F. Silvearv, A. Blomqvist, R. H. Scheicher, S. Lebégue, Ahuja, R.  
Phys. Rev. B **79**, 132102 (2009).
- III *An ab-initio study of (Mn,Al) doped ZnO including strong correlation effects*  
F. Silvearv, A. L. Rosa, S. Lebégue and R. Ahuja  
Physica E : Low-dimensional Systems and Nanostructures (2010).
- IV *Tuning magnetic properties of  $\text{In}_2\text{O}_3$  by control of intrinsic defects*  
L. M. Huang, C. Århammar, F. Silvearv and R. Ahuja  
Europhysics Letters **89**, 47005 (2010).
- V *Understanding the catalytic effects of  $\text{H}_2\text{S}$  on CVD-growth of  $\alpha$ -alumina : Thermodynamic gas-phase simulations and Density Functional Theory*  
A. Blomqvist, C. Århammar, H. Pedersen, F. Silvearv, S. Norgren, and R. Ahuja  
Accepted in Surface and Coatings Technology
- VI *Electronic structure from first principles of  $\text{LiBH}_4 \cdot \text{NH}_3$ ,  $\text{Sr}(\text{NH}_2\text{BH}_3)_2$  and  $\text{Li}_2\text{Al}(\text{BH}_4)_5 \cdot 6\text{NH}_3$  for hydrogen storage applications*  
M. Ramzan, F. Silvearv, S. Lebégue, Ahuja, R.  
Accepted in J. of Phys. Chem C
- VII *A theoretical study of point defects incorporated into CVD-grown  $\alpha$ - $\text{Al}_2\text{O}_3$*   
C. Århammar, F. Silvearv, S. Norgren, H. Pedersen and R. Ahuja  
In manuscript

Reprints were made with permission from the publishers.



# Contents

Introduction .....	ix
Part I: Theory .....	11
1 Theoretical Models .....	13
1.1 The Schrödinger Equation .....	13
1.2 Density Functional Theory (DFT) .....	14
1.2.1 Kohn-Sham formalism .....	15
1.2.2 Exchange-correlation functionals .....	16
2 Canonical quantization .....	17
3 Electron Correlations and Hubbard U .....	19
4 Electronic Structure and Magnetism in Oxides .....	21
4.1 Transition metal ion in a crystal .....	21
Part II: summary of the papers .....	25
5 Mn,Al co-doped ZnO .....	27
6 Defect-induced ferromagnetism in pure and Cr doped $\text{In}_2\text{O}_3$ .....	30
7 Hydrogen Storage Materials .....	37
7.1 $\text{LiNH}_2\text{BH}_3$ and $\text{NaNH}_2\text{BH}_3$ .....	37
7.2 $\text{LiBH}_4 \cdot \text{NH}_3$ , $\text{Sr}(\text{NH}_2\text{BH}_3)_2$ and $\text{Li}_2\text{Al}(\text{BH}_4)_5 \cdot 6\text{NH}_3$ .....	39
7.2.1 $\text{LiBH}_4 \cdot \text{NH}_3$ .....	40
7.2.2 $\text{Sr}(\text{NH}_2\text{BH}_3)_2$ .....	41
7.2.3 $\text{Li}_2\text{Al}(\text{BH}_4)_5 \cdot 6\text{NH}_3$ .....	43
7.3 Molecular dynamic simulations .....	44
8 Chemical Vapor Deposition Grown $\alpha\text{-Al}_2\text{O}_3$ .....	50
8.1 The Catalytic Mechanism of $\text{H}_2\text{S}$ .....	50
8.1.1 AlO- and AlO:Cl-surface .....	50
8.1.2 Surface reactions .....	51
8.2 Possible Point Defects .....	52
9 Conclusions and Outlook .....	56
Summary in Swedish .....	57
Acknowledgements .....	59
References .....	60





# Introduction

The work in this thesis is about functional materials in three different technological areas, spintronics, hydrogen storage, cutting tools.

Spintronics is a relatively new research field combining magnetism and electronics. The basic concept of spintronics is the manipulation of spin currents, in contrast to mainstream electronics in which the spin of the electron is ignored and only the charge of the electron is used. Adding the spin degree of freedom provides new effects, new capabilities and new functionalities. Compared with existing charge-based microelectronics technology, the ability to control and manipulate the dynamics of both carrier charge and spin by external electric and magnetic fields (as well as light) is expected to lead to novel spintronics applications. Paper III deals with zinc oxide (ZnO) co-doped with Manganese and aluminum. The idea behind this doping is to introduce a magnetic moments in a semiconductor by partially replace some cations (Zn in this case) by a transition metal (Mn). This type of semiconductor device is called a diluted magnetic semiconductor or DMS for short. Currently ZnO-based materials have been receiving considerable attention due to the specific electrical, optical and acoustic properties, which has many applications such as light-emitting diodes, laser diodes and detectors for UV wavelength range. Therefore, great experimental efforts have been devoted to synthesize ZnO-based DMS materials. However, experimental works on ZnO-based DMS materials have been highly conflicting. For example, Co-ZnO, Ni-ZnO, and Mn-ZnO were found to be paramagnetic, while others reported ferromagnetism in some samples Co-ZnO, Mn-ZnO both in bulk as well as in thin film form. Several recent studies on Mn-ZnO have shown that ferromagnetism depends strongly on methods and conditions used in the preparation of samples. Magnetic ordering in ZnO-based DMS appears to be sensitive to chemical ordering of the transition metal (TM) dopants and defects such as vacancies and interstitials. Spintronics applications require that ferromagnetism has an intrinsic origin, i.e., not from magnetic TM atom clusters or impurity phases. A fundamental understanding of the magnetic properties and nanostructures of the ZnO DMSs is crucial for the development of spintronics devices.

Furthermore, unusual ferromagnetism with high Curie temperature and big net magnetic moments have been observed in many semiconductors without any addition of TM ions. In papers I and IV a well known such material,  $\text{In}_2\text{O}_3$ , is investigated, doped and undoped, concerning various intrinsic defects influence on ferromagnetism. According to our theoretical calculations the p-type defects, especially the metal/cation vacancy, show a stable ferromagnetic coupling.

Hydrogen storage materials are a vital part of a new possible hydrogen economy proposed to replace today's fossil fuel based infrastructure as an energy carrier. Today's energy and transport economy is mainly depending on fossil fuels such as coal, oil and natural gas. In the light of today's increasing awareness about climate change and the so called "peak oil" event an intensive search for alternatives is underway. Alternative

technologies and materials have been known for decades but have never been able to successfully compete with conventional technology for various reasons. Hydrogen is an attractive energy carrier because it is easily renewable and non polluting. However, the problem of storing hydrogen in a safe and efficient way has limited its practical use as fuel for mobile applications.

The storage of hydrogen can be done in several ways such as stronger materials for containers, sorbents, and hydrides. Much research have been done on materials such as metal organic framework (MOF) or silane ( $\text{SiH}_4$ ) and its derivatives ( $\text{SiH}_4(\text{H}_2)_2$ ). Also, lightweight element hydrides have attracted special interest because they have been estimated to be the most promising materials to meet the goal of high gravimetric and volumetric storage capacity. A particular effort is put nowadays on boron-nitrogen-hydrogen compounds because they offer high hydrogen storage capacities, together with reasonable dehydrogenation performances. Papers II and VI are focusing on structure and energetic properties of metal doped boron-nitrogen-hydrogen compounds.

Paper V and VII discuss the growth of aluminum oxide  $\text{Al}_2\text{O}_3$  in the context of chemical vapor deposition (CVD). For decades the industry have been using CVD for production of wear resistant coatings on high performance cemented carbide cutting tools. Among the more common coating materials are titanium carbide and titanium nitride  $\text{Ti}(\text{C},\text{N})$  and  $\text{Al}_2\text{O}_3$ . A very attractive feature of  $\text{Al}_2\text{O}_3$  is the great chemical stability at high temperature and the relatively small thermal conductivity that will provide a more effective thermal protection for the substrate than  $\text{Ti}(\text{C},\text{N})$ . This property of  $\text{Al}_2\text{O}_3$  enables higher cutting speeds while minimizing undesirable plastic deformation of the cutting tool edge.

As far back as 1985 it was showed for the first time that  $\text{H}_2\text{S}$  increases the growth rate of  $\text{Al}_2\text{O}_3$  and at the same time result in a more homogenous growth on flanks and edges of a cutting tool edge. But the exact working mechanism have not been known even though some investigations have been done. In Paper V we conclude, among many things, from thermodynamical modeling and ab initio modeling that  $\text{H}_2\text{S}$  acts as a true catalyst on the  $\text{Al}_2\text{O}_3$  surface. We also suggest a mechanism for the catalytic mechanism. Moreover, it is demonstrated that the  $\text{AlO}$ -surfaces is thermodynamically and dynamically stabilized as it is terminated by chlorine or, in the oxygen surface case, hydrogen present in the reactor. Another issue looked into, in paper VII, was possible point defects formed as a result of the CVD reaction. In the CVD reactor there are many different molecule species that can contribute to point defects such as C, Cl, H, and S. So far our calculations show that it is energetically disadvantageous for defects to form. That is in line with measurements that show samples of CVD grown  $\text{Al}_2\text{O}_3$  to be of very pure nature even though very small amounts of defects are very hard to detect.

The thesis is outlined as follows: In part I the theoretical methods, in particular DFT is described, but also a brief description about 3d orbital splitting that occur to a transition metal in an oxide crystal. A summary of the obtained results are presented in part II.

## Part I: Theory



# 1. Theoretical Models

## 1.1 The Schrödinger Equation

To calculate the properties of materials everything begins with the Schrödinger equation [1] [2].

$$\hat{H}_{tot}\Psi_{tot} = E_{tot}\Psi_{tot} \quad (1.1)$$

$\hat{H}$  is called the Hamiltonian of the system and is the sum of the operators for kinetic energy and potential energy for all particles in the system e.i nuclei and electrons.

$$\hat{H}_{tot} = T_n + T_e + V_{ne} + V_{ee} + V_{nn} \quad (1.2)$$

$T_n$  and  $T_e$  are nuclear and electronic kinetic energy terms, respectively,  $V_{ne}$  is the nuclear-electronic coulomb attraction.  $V_{ee}$  and  $V_{nn}$  are the electron-electron and nuclear-nuclear coulomb repulsion potentials, respectively.  $\Psi_{tot}$  is the total wave function for all particles.

The time-independent, non-relativistic form is of particular interest here and it can only be solved analytically for one and two particle systems like hydrogen and atoms isoelectronic to hydrogen. So approximations have to be done and the first one is called the Born-Oppenheimer approximation, which takes note of the great difference in mass of electron and nuclei. Therefore, the electron responds almost instantaneously to any displacement of the nuclei. So instead of solving the Schrödinger equation for all particles simultaneously, the nuclei are regarded as fixed and the electrons as moving in a static electric potential arising from the nuclei. In the electronic Schrödinger equation, the new Hamiltonian  $\hat{H}$  contains only potentials for the electrons in the field of the stationary nuclei, electron-electron and nuclei-nuclei repulsion.

$$\hat{H}_e = T_e + V_{ne} + V_{ee} + V_{nn} \quad (1.3)$$

In this form the nuclei-nuclei repulsion energy becomes a constant and can be excluded when calculating the electronic energy.

$$\hat{H}_e\Psi_e = E_e\Psi_e \quad (1.4)$$

The total energy  $E_{tot}$  is the sum of the total electronic energy and nucleus-nucleus repulsion energy for a particular stationary nuclear configuration. Since the nuclei are fixed the nuclear repulsion energy is a constant and is added later when the total electron energy has been calculated. From this approximation arise the concept of potential energy curves for diatomic molecules (i.e. energy as a function of the inter-nuclear distance) and energy surface for polyatomic molecules and that the molecular geometry can be derived. The Born-Oppenheimer approximation is very reliable for

electronic ground states, but is less reliable for excited states. Now, to be able to do the calculation, the electronic wave function  $\Psi$  must be known. To find the best wave function, *variation theory* is used, which says that the solution for an approximate wavefunction always is higher in energy than for the exact solution.

$$\langle \Psi_{trial} | \hat{H}_{trial} | \Psi_{trial} \rangle = E_{trial} \geq E_0 = \langle \Psi_0 | \hat{H} | \Psi_0 \rangle \quad (1.5)$$

Where  $E_0$  is the exact ground state energy. So to find the lowest energy comes down to finding the wave function which minimizes  $E$ .

$$\min_{\Psi \rightarrow \Psi_0} E(\Psi) \rightarrow E_0 \quad (1.6)$$

And thus the energy calculated is an upper bound to the energy of the ground state. The wave function contains all the information about the system, so to extract this information one need only to apply the right operators to the wave function. However, finding the exact wavefunction is a many-body problem which comes with the problem of huge computational effort for larger systems. Finding a way to systematically map the many-body problem onto a single-body problem is thus appealing.

## 1.2 Density Functional Theory (DFT)

The density functional approach expresses ground-state properties such as electronic energy, equilibrium positions, and magnetic moments in terms of the electron density ( $\rho$ ) and thus avoids the problem of how to determine the ground wave function. The proof that this relationship between electron density and other electron properties exists is called the *Hohenberg – Kohn theorem* [1] [2]. However, it does not tell of the explicit form, just that such a functional exists. For a system with  $n$  electrons,  $(\rho(\vec{r}))$ , denotes the total density at a position  $r$ . The total energy,  $E(\rho)$ , is made up of various energy contributions:

$$E_0(\rho) = T(\rho) + E_{ne}(\rho) + E_{ee}(\rho) \quad (1.7)$$

where  $T(\rho)$  is the kinetic energy,  $E_{ne}(\rho)$  is the energy due to nuclear-electronic attraction and  $E_{ee}(\rho)$  is the classical coulomb repulsion between electrons. The second term makes it possible to apply the variational principle, so any trial density,  $\rho$ , will have a higher energy than the true density  $E(\rho) \leq E(\rho_{trial})$ . This makes it possible to directly determine the exact electron density and energy. As said before, the explicit functional relationship between energy and density is not known and it has also been very difficult to find good approximations, specially for the kinetic energy, so until recently it had little practical application. The first attempt to formulate an DFT approach was done by *Thomas* and *Fermi* but their theory treated kinetic energy in a very crude way and neglected the exchange-correlation energy. But it served as an starting point for a more advanced treatment by *Hohenberg*, *Kohn*, and *Sham*.

### 1.2.1 Kohn-Sham formalism

The basic idea in the Kohn-Sham (KS) formalism is to split the kinetic energy functional into two parts, one which can be calculated exactly and a correction term.

The exact ground-state electronic energy  $E$  of an  $n$ -electron system can be expressed as

$$E[\rho] = -\frac{\hbar^2}{2m_e} \sum_{i=1}^n \langle \psi_i^*(r_1) | \Delta_1^2 | \psi_i(r_1) \rangle - \sum_{I=1}^N \int \frac{Z_I e^2}{4\pi\epsilon_0 r_{I1}} \rho(r_1) dr_1 + \frac{1}{2} \int \frac{\rho(r_1)\rho(r_2)e^2}{4\pi\epsilon_0 r_{12}} dr_1 dr_2 + E_{XC}[\rho] \quad (1.8)$$

Where the first term is the exact kinetic energy for the non-interacting electrons, the second term is the coulomb attraction between electrons and nuclei and the third term is the classical electron-electron coulomb repulsion energy. The last term is the *exchange – correlation energy* that contains all the non-classical electron-electron interactions i.e. the correction term from kinetic energy etc. The one-electron spatial orbitals  $\phi_i$  ( $1, 2, \dots, n$ ) are called the *Kohn – Sham orbitals* and are solutions to the *Kohn – Sham equations* (KS) which can be derived by applying a variational principal to Eqn. 2.8 with the electron density given by

$$\rho(r) = \sum_{i=1}^n |\psi_i(r)|^2 \quad (1.9)$$

The KS equation for the one electron orbitals has the following form

$$\left\{ -\frac{\hbar^2}{2m_e} \Delta_1^2 - \sum_{I=1}^N \frac{Z_I}{r_{I1}} + \int \rho(r_2) r_{12} dr_2 + V_{XC}(r_1) \right\} \psi_i(r_1) = \epsilon_i \psi_i(r_1) \quad (1.10)$$

where  $\epsilon_i$  are the KS orbital energies and the *exchange – correlation potential*  $V_{XC}$  is the functional derivative of the exchange-correlation energy:

$$V_{XC}[\rho] = \frac{E_{XC}[\rho]}{\rho} \quad (1.11)$$

If  $E_{XC}$  is known, then  $V_{XC}$  is easily obtained. The KS equations are solved in a self-consistent field (SCF) way. First, we guess the charge density  $\rho$ , and then calculate  $V_{XC}$  as a function of  $r$  by an approximate form of functional for the dependence of  $E_{XC}$  on density. Now we have a set of KS equations that are solved to obtain a set of KS orbitals. This initial set of orbitals are used to calculate a new improved density and so on until the density and  $E_{XC}$  has converged to some tolerance level. The KS orbitals can be computed numerically or expressed with basis functions. The above formalism was for paired electrons that have the same spatial one-electron orbital analogous to restricted HF. For spin dependence the Kohn-Sham formulas are generalized to a spin-polarized system, that is, to allow for the electrons with different spin to have different spatial density. The Kohn-Sham equation is replaced by a pair of equations, one for each spin. This is analogous to unrestricted HF-theory. The computation time for DFT can generally be set as third power of number of basis functions.

### 1.2.2 Exchange-correlation functionals

Since no exact form for the exchange-correlation functional is known, several schemes have been developed to get an approximate description for the functional. This is usually where most of the error in DFT arises. A problem in DFT is that there is no systematic way of improving the approximate exchange-correlation functional like in wavefunction based methods. So one has to fall back on conceptual modelling of the exchange-correlation hole, physical intuition, and fitting experimental data. The simplest approximation model is the local density approximation (LDA)[2]

$$E_{XC} = \int \rho(r) \epsilon_{XC}[\rho(r)] d\bar{r} \quad (1.12)$$

or for the unrestricted case (LSDA)

$$E_{XC} = \int \rho(r) \epsilon_{XC}[\rho^\alpha(r), \rho^\beta(r)] d\bar{r} \quad (1.13)$$

where  $\epsilon_{XC}[\rho(r)]$  is the exchange-correlation energy per electron in a homogeneous electron gas of constant density. A homogeneous electron gas is a hypothetical model where an infinite number of electrons travel throughout an infinite space volume in which there is a uniform and continuous distribution of positive charge to retain electro neutrality. This is of course a very crude approximation for a molecule so corrections must be introduced. A common way to do that is to include gradient corrections to the local function and thus the energy depends not only on density but also on the gradient of the density, this method is called Generalized Gradient Approximation (GGA) and the expression is

$$E_{XC}[\rho^\alpha, \rho^\beta] = \int f[\rho^\alpha, \rho^\beta, \nabla \rho^\alpha, \nabla \rho^\beta] d\bar{r} \quad (1.14)$$

where  $f$  is a function of the density and its gradient at the point  $\bar{r}$ .



## 2. Canonical quantization

When Werner Heisenberg developed quantum mechanics 1925 [3] he used a procedure for quantizing a classical theory while preserving as much as possible of the formal structure of the classical theory. This is a procedure called canonical quantization that arise from the Hamiltonian approach to classical mechanics. This is commonly called first quantization for historical reasons. The canonical method was later used when Paul Dirac 1927 formulated his quantum field theory, consequently called second quantization [4]. The difference between quantum mechanics and quantum field theory is that in the later the fields and the particles themselves are quantized in addition to the motion of the particle. In quantum field theory all quantum states are assumed to be represented by state vectors in a Hilbert space, and that all observables are represented by Hermitian operators acting on this space. Operators can then be expressed as so called creation and annihilation operators  $c_i^\dagger$  and  $c_i$  since they create or annihilate particles in a specific state in a many body system. For a system with fermions i.e. electrons, they have to obey the Pauli exclusion principle and thus anticommute  $\{A, B\} \equiv AB + BA$

$$\{c_k^\dagger, c_l^\dagger\} = 0 \quad (2.1)$$

$$\{c_k, c_l\} = 0 \quad (2.2)$$

$$\{c_k, c_l^\dagger\} = \delta_{k,l} \quad (2.3)$$

$$(2.4)$$

Now we can describe the propagation of a free particle with a one particle operator description

$$T_{tot} = \sum_{k,l} T_{k,l} a_k^\dagger a_l, \quad (2.5)$$

where T is the kinetic energy and a two particle interaction with a two particle operator

$$V_{tot} = -\frac{1}{2} \sum_{k,l,i,j} V_{k,l,i,j} a_k^\dagger a_l^\dagger a_i a_j \quad (2.6)$$

where V is the Coloumb interaction potential. As an example of a how useful the second quantization description can be we define the single particle propagator Green's function as

$$G(\lambda, t - t') = -i \langle \Psi_0 | T c_\lambda(t) c_\lambda^\dagger(t') | \Psi_0 \rangle \quad (2.7)$$

The quantum number  $\lambda$  can be anything dependent on the problem studied. The Green's function describes the motion and interaction of particles and holes and can

be used to calculate a variety of different properties, for example calculating experimental spectra. Here it is written in the Heisenberg picture at zero temperature, that is to say time independent ground state wave function and time dependent creation and annihilation operators

$$c_\lambda(t) = e^{iHt} c_\lambda e^{-iHt}. \quad (2.8)$$

In the above description  $T$  is the Dyson chronological operator and  $H$  is the exact Hamiltonian of the system and  $t'$  is the start time (from here on will be set to 0) and  $t$  is the end time. More explicitly we can write Eqn. 2.7 like this

$$G(\lambda, t) = -i \langle \Psi_0 | c_\lambda e^{-iHt} c_\lambda^\dagger | \Psi_0 \rangle e^{iE_0 t} \quad t > 0. \quad (2.9)$$

$$G(\lambda, t) = i \langle \Psi_0 | c_\lambda^\dagger e^{iHt} c_\lambda | \Psi_0 \rangle e^{iE_0 t} \quad t < 0. \quad (2.10)$$

### 3. Electron Correlations and Hubbard U

As mentioned before the LDA treats the Coloumb interactions between electrons approximately as if it could be describe by a uniform electron gas . This makes the description of localized states such as d- ad f-electrons bad. One way to improve the correlation part of the correlation-exchange functional is to add an onsite Coloumb interaction to the basic LSDA functional. We start with the simplest model of interacting particles in a lattice the so called *Hubbard – model* [5, 6, 7]

$$H = \sum_{i,j\sigma} t^{ij} a_{i,\sigma}^\dagger a_{j,\sigma} + \frac{1}{2} \sum_i U_i a_{i,\sigma}^\dagger a_{i,\sigma'}^\dagger a_{i,\sigma} a_{i,\sigma'}. \quad (3.1)$$

Here the first term is the kinetic energy,  $t_{ij}$  describes an electron hopping from one site to another, the second term is the Coloumb on site term including the Coloumb  $U$ .  $ij$  denotes the crystal lattice sites,  $\sigma$  is the spin index ( $\sigma \equiv \uparrow, \downarrow$ ) . The Colomb  $U$  is the difference in energy between removing an electron from the occupied state to vacuum and that of adding a electron from a vacuum state to the unoccupied state, referenced to the energy of the unperturbed system

$$U = E(n+1) + E(n-1) - 2E(n). \quad (3.2)$$

Said in a another way, it is the energy cost of placing two electrons at the same site. The  $U$  term and its size relative the bandwidth  $W$  will determine the correlation between electrons. If  $U \ll W$  the kinetic energy part is dominant in Eqn. 3.1 and the correlation will be weak but if  $U \gg W$  then the Coloumb on site term dominates and there are a strong correlation between electrons. In the strong correlated case DFT can not give a correct description of the electron structure and in general overestimates the bandwidth, gives wrong position of bands, underestimates bandgap in semiconductors etc. Starting from LSDA, Anisimov and Lichtenstein [7] added a Coloumb onsite energy term  $E_U$  to the ordinary LSDA functional.

$$E^{LSDA+U}[\rho^\sigma(\mathbf{r}), \{n^\sigma\}] = E^{LSDA}[\rho^\sigma(\mathbf{r})] + E^U[\{n^\sigma\}] - E_{dc}[\{n^\sigma\}]. \quad (3.3)$$

Here  $\rho(\mathbf{r})$  is the charge density of electron with spin  $\sigma$ ,  $E^{LSDA}[\rho^\sigma(\mathbf{r})]$  is the original LSDA functional. The last term  $E_{dc}[\{n^\sigma\}]$  corrects for the double counting.  $E_U$  is explicitly written as

$$\begin{aligned} E^U[\{n^\sigma\}] = & \frac{1}{2} \sum_{m,\sigma} \{ \langle m, m'' | V_{ee} | m', m''' \rangle > n_{mm'}^\sigma n_{m''m'''}^{-\sigma} \\ & + (\langle m, m'' | V_{ee} | m', m''' \rangle > \\ & - \langle m, m'' | V_{ee} | m''', m' \rangle) n_{mm'}^\sigma n_{m''m'''}^\sigma \}, \end{aligned} \quad (3.4)$$

where  $V_{ee}$  are the screened Coloumb interactions among the electrons. Now, the  $V_{ee}$ 's has to be determined. We can do this by express  $V_{ee}$  in complex spherical harmonics and effective Slater integrals  $F^k$  [10]

$$\langle m, m'' | V_{ee} | m' m''' \rangle = \sum_k a_k(m, m', m'', m''') F^k. \quad (3.5)$$

The Slater integrals can be adjusted to experiment to get the correct screened Coloumb interaction. The terms  $n_{mm'}^\sigma$  and  $n_{m''m'''}^\sigma$  are density matrices, corresponding to

$$n_{m,m'} = \langle \Psi^{S'} | m' \rangle \langle m | \Psi^S \rangle \quad (3.6)$$

$$n_{m'',m'''} = \langle \Psi^{S''} | m''' \rangle \langle m'' | \Psi^{S''} \rangle. \quad (3.7)$$

The last term  $E_{dc}$  corrects for the double counting and can be approximated in several ways. Here are two examples:

*Fully Localized Limit* [8] : assumes that the total number of d (f) electrons  $N = \sum n_m$  is given properly by LDA (but not the eigenvalues)

$$E_{dc}[\{n^\sigma\}] = \frac{1}{2}UN(N-1) - \frac{1}{2}JN^\uparrow(N^\uparrow-1) + N^\downarrow(N^\downarrow-1) \quad (3.8)$$

where  $U$  and  $J$  are the screened Coloumb and exchange parameters and  $n = n^\uparrow + n^\downarrow$ . This leads to

$$V_{m,m',\sigma} = (U-J)\left(\frac{1}{2} - n_{m,m',\sigma}\right) \quad (3.9)$$

and can shift the center of bands.

*Around Mean Field Approximation* [9] :

$$E_{dc}[\{n^\sigma\}] = \frac{1}{2}UN^2 - \frac{1}{2}J\sum_\sigma N_\sigma^2 - \frac{1}{2}(U-J)\sum_\sigma n_{aver,\sigma}^2 \quad (3.10)$$

and

$$V_{m,m',\sigma} = (U-J)(n_{aver,\sigma} - n_{m,m',\sigma}) \quad (3.11)$$

which leaves the center of bands unchanged.

Orbitals with occupancies  $n_{m,m',\sigma}$  larger than 1/2 (or  $n_{average}$ ) become more populated, others become more depopulated. So to summarise, LDA+U shifts occupied states down and empty states up in energy with  $U/2$ .  $U$  and  $J$  can either be taken from experiment or estimated by various calculation methods.

## 4. Electronic Structure and Magnetism in Oxides

Magnetic oxides exhibit a whole range of both magnetic and transport properties which make them particularly interesting for spintronics applications. The large variety of physical properties that transition-metal oxides can exhibit (ferro-, ferri- and antiferromagnetism, good insulators, insulator-metal transition, metallicity, superconductivity, optical properties) could be used to design materials with certain physical properties required for a specific functionality but they are also of great importance when miniaturisation drives the need for materials that can do more than one task. Usually the same electrons are responsible for both magnetic and electric properties and therefore an interdependence is often seen between them in experiments.

### 4.1 Transition metal ion in a crystal

A free isolated ion with partially filled 3d orbitals has a 5-fold degeneracy. Electrons will fill up these levels according to Hund's rule to minimize the coulomb repulsion. As a consequence a state with maximum possible spin will be formed. When the ion is placed in a crystal the surrounding ions will affect it and the symmetry is broken so some of the degeneracy will be lifted and what is called an orbital splitting will occur. How the five 3d-levels will be modified depends on the symmetry of the surroundings. A first qualitative analysis of this splitting is done by a so called crystal field (CF) model. The CF is a simplified model where the surrounding ions have been replaced by point charges. Figure 4.1 shows some d-orbital splitting for three types of common symmetries: octahedral, tetrahedral and square planar.

As seen from Fig. 4.1 the splitting can be explained by looking at how the orbital lobes are directed. In the octahedral case the  $e_g$  orbital lobes are directed towards the negatively charged ligands so they experience a stronger coulomb repulsion than the lobes that are directed between them ( $t_{2g}$ ). There is also another contribution to the splitting not seen in the CF model. If we combine CF theory with molecular orbital theory we get a more realistic theory from which we can see that there is another contribution to the splitting besides the coulomb repulsion called covalency contribution. This contribution comes from hybridization of overlapping p-d. A large overlap and consequently large mixing of the orbitals gives a higher energy of the d-orbital than a small overlap.

If we now consider the octahedral splitting and we have four d electrons, where would we put the fourth electron? It could be placed spin parallel to the other electrons according to Hund's rule but then we have to place it on a higher energy level or it could be placed antiparallel on one of the lower energy orbitals. Which state that is more stable compared to the other is determined by the ratio of the CF splitting energy

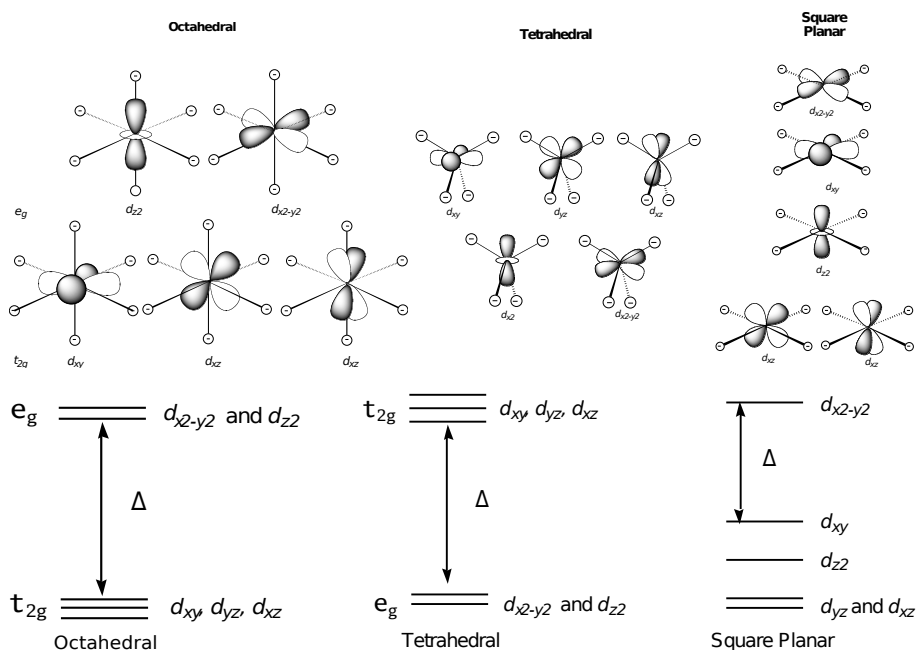


Figure 4.1. An illustration of the CF model. It shows the direction of different d-orbitals and the surrounding point charges. Below are the corresponding energy diagrams.

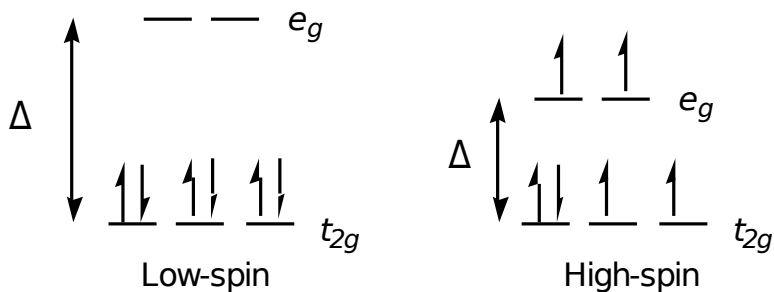


Figure 4.2. An example of high-spin and low-spin configuration.

and the onsite ferromagnetic energy exchange interaction  $-J_H \sum_{\alpha,\beta} \mathbf{S}_{i\alpha} \mathbf{S}_{i\beta}$  where  $i$  is the site index and  $\alpha, \beta$  are indices of different d-orbitals. If  $\Delta_{CF} < J_H$  then a low spin state would form and if the opposite case were true then a high spin state would be the most stable state, see Fig. 4.2.

The High spin state is the most common state among TM oxides with the exceptions of  $\text{Co}^{3+}$  ( $d^6$ ),  $\text{Ni}^{3+}$  ( $d^7$ ) and  $\text{Ru}^{4+}$  ( $d^4$ ) that are often of low spin state. The spin state is also affected by parameters such as temperature, pressure, composition. A change from one spin state to another have also the capability to induce a phase transition.





**Part II:**  
summary of the papers



## 5. Mn,Al co-doped ZnO

In paper I we have done a first principles calculation where strong correlation effects included to Mn,Al co-doped ZnO. The motivation for this study is that existing calculations [12, 13, 15, 16], which predicts a hole mediated-carrier model for ZnMnO (p-type system) and that carriers in n-type ZnMnO will not delocalize into Mn ion instead of remaining in the conduction band or donor levels. However, these calculations have ignored the strongly correlated nature of the Mn d electrons. It is of great importance that the position of the d states are correct, since they will hybridize with the Al states and this will ultimately control the superexchange in this system. The question is whether the double exchange mechanism, which promotes ferromagnetism, will overcome the superexchange interaction. Theoretical results contradicts experiments where strong correlation between Curie temperature and intrinsic defects [14, 11, 19, 18] or impurities [17] has been reported in Mn-doped ZnO samples. The introduction of carriers has been achieved experimentally [19], and both oxygen vacancy and Al co-doping introduced a ferromagnetic behaviour. This is another reason for doing a more correct theoretical study. Fig. 5.1 shows ZnO with two Zn ions replaced by two Mn ions and also the different Al positions 1-6 that been tested to evaluate the magnetic exchange interaction. The magnetic ordering was determined by calculate the difference between the ferromagnetic and antiferromagnetic state. The result is presented in Fig. 5.2.

From Fig. 5.2 we can see that for all configurations (Mn,Al) ZnO is strongly AFM, with differences in energy between the two magnetic states being between -60 meV and -80 meV depending on the position of the Al atom. Therefore, we can conclude that the magnetic state of the Mn ions is weakly modified by the extra electron introduced by Al, and is independent of the position of the Al atom in the cell.

This result can be further confirmed in our calculated density of states (DOS) shown in Fig. 5.3. The host valence band is mainly made of Zn 3d states ranging from -8 eV to -6 eV and the O 2p states from -8 to -2 eV. The Mn 3d occupied states span a region from -7.5 to -2 eV with the Mn 3d states being 100 % polarized. We observe a strong hybridization between the Mn 3d states and the O 2p states around -2.5 eV, but the hybridization between the Al states and the Mn 3d states is weak, so it becomes clear that the Al atom is giving its electron to the ZnO host. As a consequence, the occupation of the Mn 3d states is not modified (the magnetic moment is still close to  $5\mu_B$ ) and the double exchange mechanism between Mn atoms cannot be realized. Therefore, the introduction of electrons by Al doping cannot explain the appearance of ferromagnetism in (Mn,Al)ZnO. However, it may be possible that ferromagnetism occurs in the presence of other defects, such as Zn or O vacancies induced by Al doping. Further experimental work is needed to elucidate completely the mechanisms involved in this system.

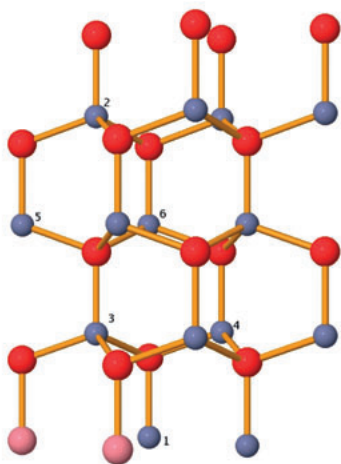


Figure 5.1. A wurzite ZnO supercell (2x2x2), blue is Zn, red is oxygen and pink Mn atoms. Al atom replace Zn on labeled sites 1-6.

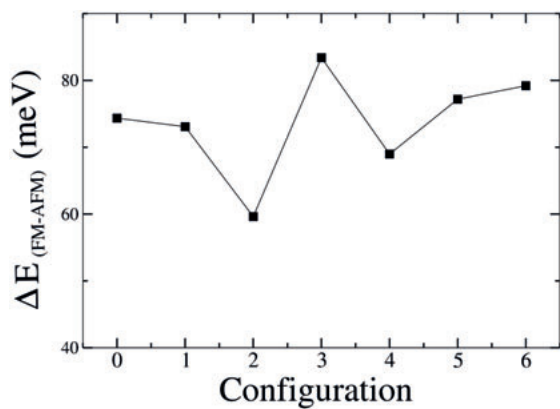
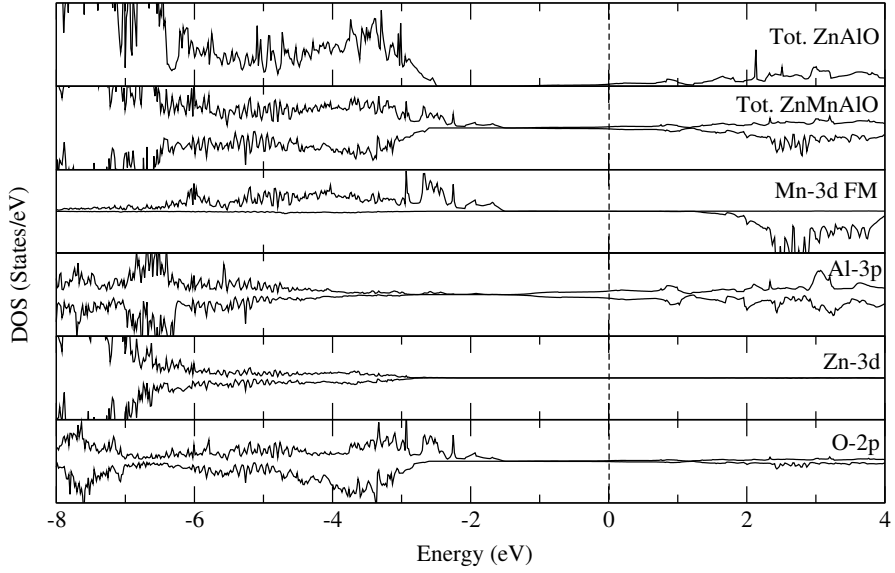


Figure 5.2. The total energy difference between FM and AFM states plotted against different Al sites in (Mn,Al)ZnO. All the difference in energy are positive and corresponds to an antiferromagnetic ground state. Configuration “0” corresponds to ZnOMn without Al doping.



*Figure 5.3.* Total DOS of ZnAlO and total and partial DOS in (Mn,Al)ZnO with GGA+U ( $U=4$  eV) calculation. The O ion indicated by partial DOS is adjacent to Mn a ion. The dotted line indicates the Fermi level. The Al atom is in position 1 (See Fig. 5.1.)

## 6. Defect-induced ferromagnetism in pure and Cr doped $\text{In}_2\text{O}_3$

In paper I and IV first principle calculations of four kinds of intrinsic point defects have been studied on two different systems with similar properties. From both experimental and theoretical studies there is a common agreement that intrinsic defects play an important role for the ferromagnetism in Diluted Magnetic Semiconductors (DMS) [20, 21, 22, 23]. However, there exists a discrepancy between experiments and calculations regarding the character of these defects, some experiments find a correlation between ferromagnetism and conduction electrons [24, 25, 26] but theoretical calculations instead show that p-type and not n-type defects are the ones that are likely to induce long-range ferromagnetism in DMS.

Fig. 6.1 shows the calculated density of states for the ground state of  $\text{In}_2\text{O}_3$  (IO), containing various neutral defects. The first thing one can see is that the relative position of the Fermi energy shows that  $V_O$  and  $\text{In}_I$  act as shallow donors while  $O_I$  and  $V_{In}$  act as shallow acceptors. Secondly, the ground states of two p-type defects are spin-polarized, while the ground states of two n-type defects are non-spin-polarized. The total magnetic moment induced by each p-type point defect is equal to the number of holes, i.e. 3 and 2  $\mu_B$  for  $V_{In}$  and  $O_I$ , respectively.

In Fig. 6.2 are the carrier density of IO presented with various neutral defects,  $O_I$ ,  $V_{In}$ ,  $V_O$ , and  $\text{In}_I$ . The isosurfaces of  $0.02 \text{ e}\text{\AA}^{-3}$  are shown for all the carrier densities. From the figure we can see that the shape of the isosurface for the holes has an obvious p-orbital character, while the isosurface for the electrons has a spherical s-orbital character.

Fig. 6.3 shows the spatial distribution of spins in one cubic unit cell of IO with p-type point defects,  $O_I$  and  $V_{In}$ . First, almost all of the magnetic moments are located at oxygen sites. For the  $O_I$ , 43% of the magnetic moments reside on the  $O_I$  site, while for the  $V_{In}$  case, 66% of the magnetic moments are distributed on the six O nearest neighbours (NN) of the  $V_{In}$  site. The magnitude of the magnetic moments decrease with the distance from the point defect site. Both p-dopants cause electron deficiency in the three delocalized p-orbitals of the oxygens, leading to the formation of local moments. In the case of the n-type  $V_O$ , it instead introduces additional electrons. These electrons will fill up the empty 5s-like state of In, which has a singlet ground state.  $\text{In}_I$  could in principle contribute with a moment of 1  $\mu_B$ , due to the singly occupied 5p-state. However, according to our calculations the magnetic moment due to  $\text{In}_I$  is 0  $\mu_B$ . This is not an intuitive result, and could be related to the overestimation of charge delocalization by GGA.

The calculated formation energies of the four neutral defects, as can be seen in Table 6.1, is quite high, and thus a non-equilibrium enhancement factor is needed in order to achieve a defect concentration high enough to observe magnetic ordering. The calculated formation energies of the p-type defects in their most stable charge states

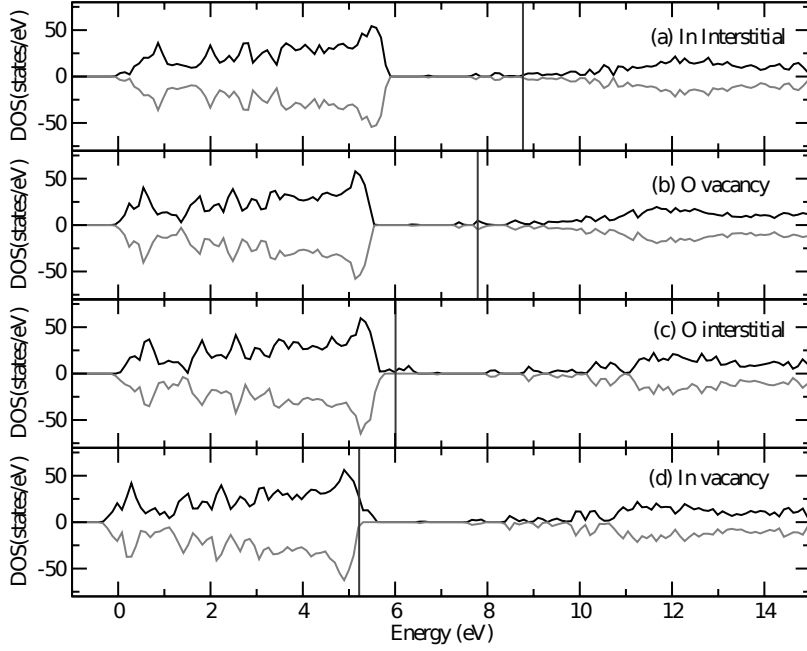


Figure 6.1. Spin-resolved total density of states (DOS) for  $I_O$  with various native defects. The valence band minimum is set to 0. The vertical solid lines denote the Fermi energies for each defect conditions.

Growth condition	$\Delta H$ ( $V_{In}$ )	$\Delta H$ ( $O_i$ )	$\Delta H$ ( $In_i$ )	$\Delta H$ ( $V_O$ )
O rich, In rich	8.7	4.3	5.2	4.0
O rich, In poor	4.8	4.3	9.1	4.0
O poor, In rich	8.7	6.9	5.2	1.4

**Table 6.1.** Calculated formation energies  $\Delta H$  (eV) for various neutral defects in different experimental sample growth conditions.

have been calculated as a function of Fermi energy  $E_F$ . This can be seen in Fig. 6.4. The formation energy of p-type defects can be greatly decreased by the the formation of their negative charge states, which means that the p-type defects are most likely formed if a high-energy electron reservoir is given. However, the hole states created by the p-type defects will be compensated and simultaneously, the magnetic moments will disappear. One way to favour formation of negatively charged p-type defects in thin coatings of  $In_2O_3$ , is to pin the Fermi energy closer to the CBM by depositing  $In_2O_3$  on a Si-substrate. Alternatively, certain TM, such as Sn, Mo, V and Cr, acting as n-type electron donors, can induce the formation of negatively charged intrinsic defects by charge transfer from electron donors to unfilled acceptor states.

For Cr-doped  $I_O$ ,  $E_F$  is close to the minimum of conduction band. As is seen from Fig. 6.4, when  $E_F$  is in this energy range, the formation energy of both p-type defects,  $O_I$  and  $V_{In}$ , in the negative charge state is found to display negative values under

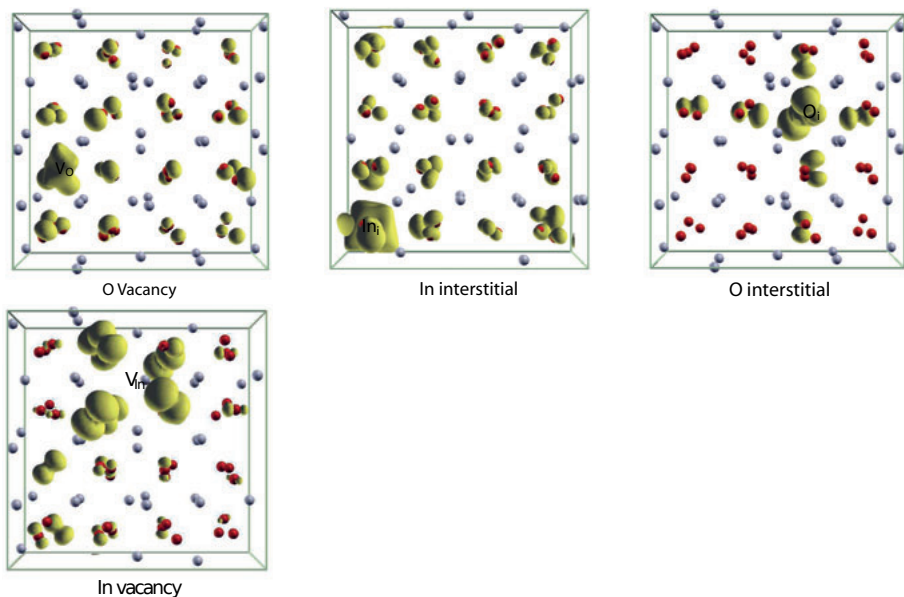


Figure 6.2. The carrier spatial distributions for intrinsic neutral defects O vacancy, In interstitial, O interstitial and In vacancy. The red and grey spheres represent the O and In ions, respectively. The yellow spheres represent the isosurface of  $0.02 \text{ e}\text{\AA}^{-3}$

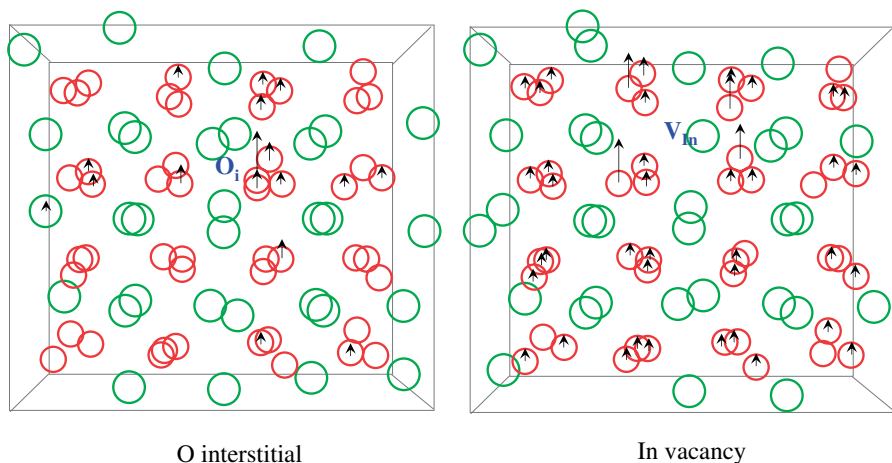


Figure 6.3. The spin spatial distribution in one cubic unit cell of p-type defect: (a) O interstitial, (b) In vacancy doped IO. The red (black) circles represent the position of oxygen ions, the green (grey) circles represent the positions of In ions. The arrows on each atomic position represent the spin on each ion site, which is integrated within the radius of oxygen or In ions. The ionic radius of oxygen is taken as  $1.24 \text{ \AA}$ , and the ionic radius of In is taken as  $0.94 \text{ \AA}$ .





	$\Delta E$ (eV) (“close”)	$\Delta E$ (eV) (“far”)	M/Cr ( $\mu$ B)
$V_O$	-0.003	0.001	3.0
$In_i$	0.074	-0.030	3.0
$V_{In}$	0.340	0.250	1.5
$O_i$	0.540	0.120	2.0

**Table 6.2.** Total energy difference  $\Delta E = E_{AFM} - E_{FM}$  and total magnetic moment per Cr atom for 6% Cr-doped  $I_O$  with various defects. Here “close” and “far” represent two Cr atoms at close (3.34 Å) or far (7.15 Å) separation distance, respectively.

O-rich growth conditions, which means that p-type defects could spontaneously be formed. The concentration of such defects would then be controlled by the available impurity electrons. Overall, as can be seen, the p-type defects have a great possibility to be formed in Cr-doped IO even in O-deficient reduction reaction growth conditions (when  $E_F$  is located close to the CBM).

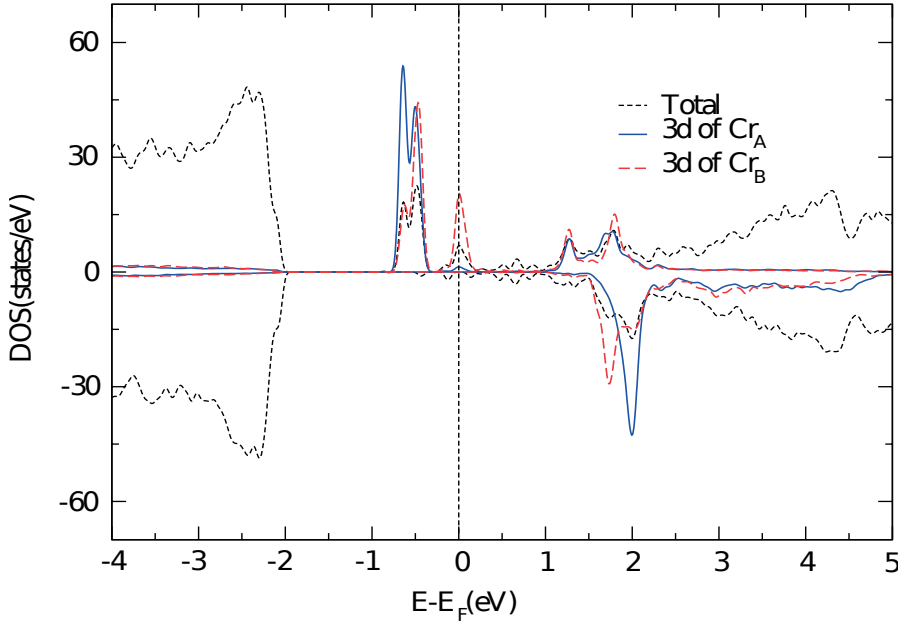


**Figure 6.5.** Spin-resolved total and partial electron density of states (DOS) of 6% Cr-doped  $In_2O_3$  in the ferromagnetic configuration. Here one of Cr atom sits at the A site, and another Cr atom sits at the B site. The A and B sites have been defined in the text. The partial DOS is scaled compared to the total DOS.

The density of states (DOS) of Cr-doped  $I_O$  in the ferromagnetic configuration is shown in Fig. 6.5. The Cr 3d electrons are totally spin polarized, occupying the spin-up channel. The distorted octahedral crystal field formed by the O anions splits the Cr 3d band into a threefold  $t_{2g}$ -like band in the lower energy range and a twofold  $e_g$ -like band in the higher energy range.

The ferromagnetic stability is determined by the total energy difference ( $\Delta E$ ) between the antiferromagnetic (AFM) and ferromagnetic (FM) configurations. In Table 6.2 the calculated differences between FM and AFM states are shown. The FM configuration is found to be 0.07 eV/cell lower in energy than the AFM configuration for the Cr-Cr distance of 3.34 Å. A spin-glass-like ground state or AFM ground state is found for further Cr-Cr separations. The calculation of critical temperature for DMS materials using Monte Carlo simulations [27] has shown that the ferromagnetic exchange interaction between those magnetic ions at an average distance, for a given impurity concentration, plays a key role in inducing the high  $T_c$  instead of near exchange interaction. Thus without introducing other defects, Cr-doped IO has no possibility to reach the experimentally observed high  $T_c$ .

Both p-type defects have a great efficiency in inducing unusually large ferromagnetic coupling for the two Cr-Cr distances, which is not achieved by the n-type defects. The total and partial DOSs for the systems with the four native defects ( $V_O$ ,  $In_i$ ,  $V_{In}$ , and  $O_i$ ) are shown in Fig. 6.6 (a)-(d). As is seen from Fig. 6.6 (a) and (b), the impurity bands formed by  $V_O$  and  $In_i$  are very close to the occupied Cr 3d band. The unoccupied Cr 3d  $e_g$ -like states are in the higher energy range of the conduction band. The donor states formed by  $V_O$  or  $In_i$  are lower than the unoccupied Cr 3d states. In this situation, there is no possibility for charge transfer from the donor to the magnetic cation. Thus, the model of donor-mediated ferromagnetism [22] could not be applied to the current system.

As is seen from Fig. 6.6 (c) and (d), the hole bands introduced by the p-type defects are close to the maximum of the valence band and are located at much lower energy than the Cr 3d states. Thus, charge transfer from Cr 3d states to the these hole states is energetically favorable. Since the valence electrons on the Cr ion are partially removed, the electronic states of Cr ions certainly become mixed valence states. This would make the double exchange interaction, involving electron hopping between magnetic anions in the mixed valence state [21] a plausible mechanism for this unusually strong ferromagnetism.

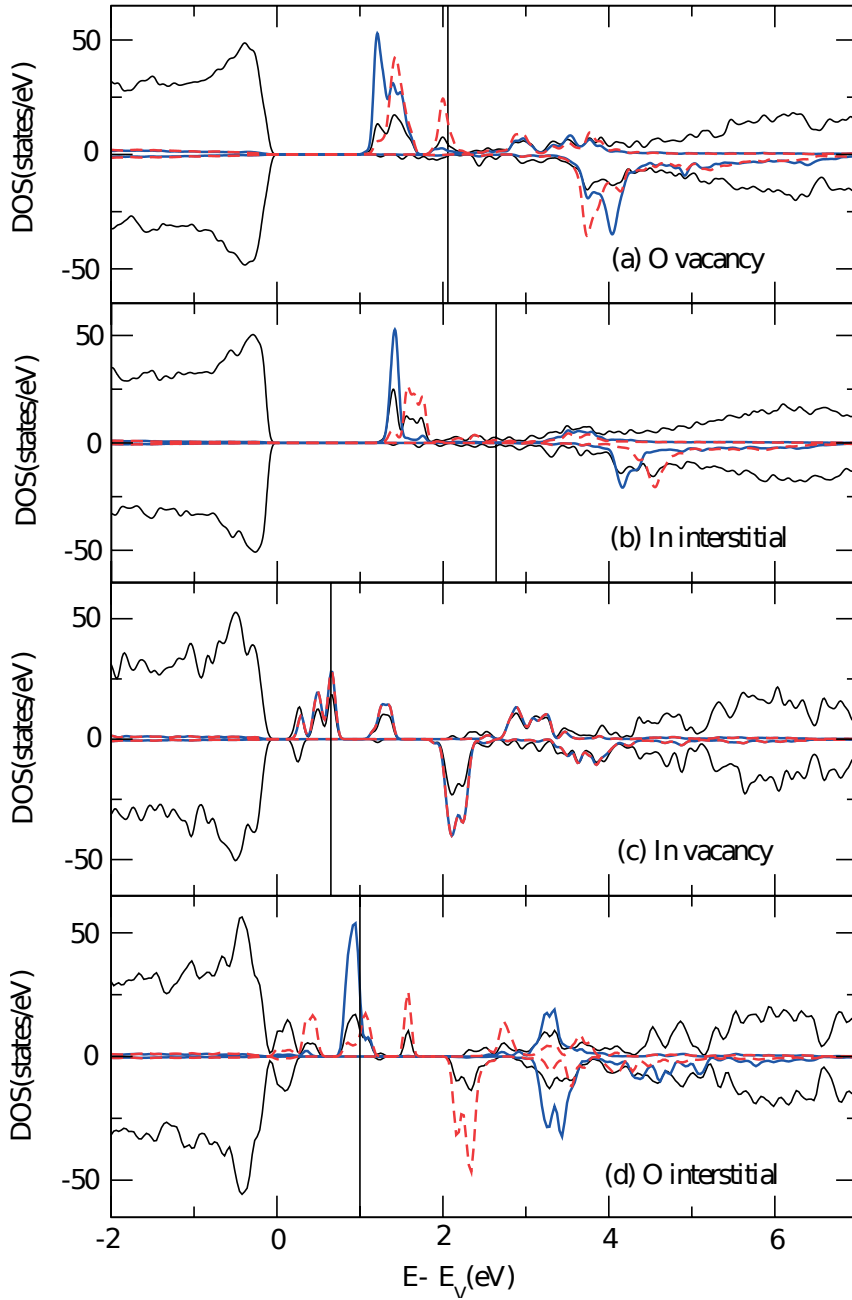


Figure 6.6. Spin-resolved total DOS and partial electron DOS of 6% Cr- doped  $\text{In}_2\text{O}_3$  in the FM configuration with additional defects: (a) O vacancy, (b) In interstitial, (c) In vacancy, and (d) O interstitial. The solid black line represents the total DOS, the blue and dashed red lines represent the partial DOSs of the two Cr 3d states. The partial DOSs are scaled compared to the total DOS. The zero energy level is set at the maximum of the valence band. Fermi levels are represented by the solid vertical lines.

## 7. Hydrogen Storage Materials

We have studied the properties of different hydrogen storage materials based on ammonia borane. Ammonia borane,  $\text{NH}_3\text{BH}_3$ , is a very interesting material as a chemical hydrogen storage material, mainly due to its favorable gravimetric and volumetric properties [28] - [32]. The problem is that a release of hydrogen results in polymerization to  $(\text{NH}_2\text{BH}_3)_n$  and eventually to  $(\text{NHBH})_n$  upon further heating [28] - [32]. This polymerization makes the rehydrogenation problematic. Another problem is that the released hydrogen is contaminated with aminoborane and trace quantities of borazine which will poison the fuel cell. A solution to the problem may be to replace a hydrogen with some other light cation to form metal amidoborane.

### 7.1 $\text{LiNH}_2\text{BH}_3$ and $\text{NaNH}_2\text{BH}_3$

In paper II we investigated two such materials namely,  $\text{LiNH}_2\text{BH}_3$  and  $\text{NaNH}_2\text{BH}_3$  that were synthesized by Xiong et al. [33]. They can release hydrogen at easily accessible temperatures without the unwanted contaminate borazine [33].

We performed a theoretical test to see how stable the *Pbca* phase of  $\text{LiNH}_2\text{BH}_3$  might be against competing structures and further we also investigated other possible candidate phases. A list of possible space groups were tested and their respective total energy difference in eV/f.u. (f.u.=formula unit) relative to the *Pbca* phase in parentheses: *Pbcn*(0.42), *Pnma*(0.48), *Pcca*(0.86), and *Pnnm* (2.27). The conclusion based on these results is that the *Pbca* structure does yield the lowest total energy and is stabilized by 0.42 eV/f.u. against the second most stable phase of *Pbcn*. The phase *Pbca* seems to be dynamically stable since no imaginary frequencies were found in the calculated vibrational spectra. The crystal structure of  $\text{LiNH}_2\text{BH}_3$  is shown in Fig. 7.1(a).

To understand the mechanism of hydrogen release we have to look at the electronic configuration. The corresponding density of states (DOS) and partial density of states (PDOS) of  $\text{LiNH}_2\text{BH}_3$  and  $\text{NaNH}_2\text{BH}_3$  are presented in Fig. 7.2. The PDOS (second to last rows of Fig. 7.2) is used to analyze the chemical bonding between different chemical species. Similarities in the position of the peaks between the nitrogen atom and its two neighboring hydrogen atoms in their respective PDOS showing a strong bonding between them. The same analysis holds for the boron atom and the remaining three hydrogen atoms. The lithium and sodium ions have mainly ionic bondings between their neighbors since PDOS show a much weaker correlation with the PDOS of the other atoms.

The corresponding Bader charges for the two compounds investigated here are reported in Tab. 7.1. The results clearly reveal the strong ionic character of the Li/ $\text{NaNH}_2\text{BH}_3$  bonds since the alkali metal ion is seen to have lost most of its electron toward the  $\text{NH}_2\text{BH}_3$  - group.

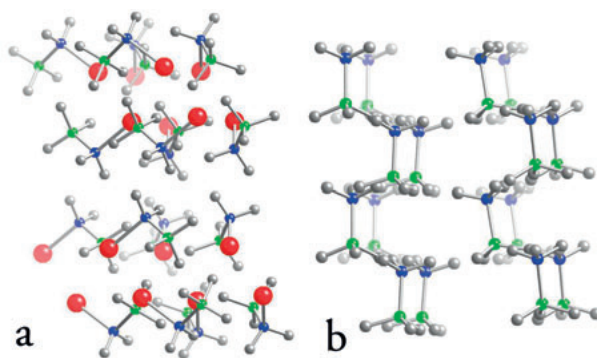


Figure 7.1. The fully relaxed crystal structures of  $\text{LiNH}_2\text{BH}_3$  ( $Pbca$ ) (a) and  $\text{NH}_3\text{BH}_3$  (b) as obtained from our density functional theory calculation. Li is shown as red spheres, N in blue, B in green, and H in grey.

atom	$\text{LiNH}_2\text{BH}_3$	$\text{NaNH}_2\text{BH}_3$
Li/Na	+0.87	+0.82
N	-1.47	-1.44
B	+1.87	+1.86
H(1)	+0.36	+0.35
H(2)	+0.36	+0.36
H(3)	-0.66	-0.65
H(4)	-0.67	-0.65
H(5)	-0.65	-0.64

**Table 7.1.** Calculated Bader atomic charges (in units of  $e$ ) for  $\text{LiNH}_2\text{BH}_3$  and  $\text{NaNH}_2\text{BH}_3$  in the  $Pbca$  structure.

Looking at the two hydrogen atoms, labeled H(1) and H(2) in Table 7.1, bonded to the nitrogen atom, one can see that they have lost a significant part of their electronic charge (the charge is +0.36 $e$ ); and the three hydrogen atoms, labeled H(3), H(4), and H(5), bonded to the boron atom, which possess a significant negative charge (about -0.65 $e$ ). Therefore, the two groups of hydrogen atoms differ by a charge of approximately one electron, reflecting the different electronegativity of nitrogen and boron atoms with charges of about -1.4 $e$  and +1.9 $e$ , respectively.

These differences will have an effect on the hydrogen removal energies as we will see. We constructed a  $2 \times 1 \times 1$  supercell of  $\text{LiNH}_2\text{BH}_3$  for the  $Pbca$  space group and proceeded to take away one hydrogen atom bonded either with boron or with nitrogen. We found that the binding energy for hydrogen at the B site is 5.63 eV and for hydrogen at the N site 6.02 eV. These numbers are rather similar to what we found in ammonia borane [Fig. 7.1(b)], namely, 5.27 eV at the B site and 5.81 eV at the N site and also follow the same trend, i.e., the N-H bonds are stronger than the B-H bonds. The similarity in the theoretical hydrogen desorption energies between  $\text{LiNH}_2\text{BH}_3$  and  $\text{NH}_3\text{BH}_3$  is in good agreement with experimental measurements [33, 31] which

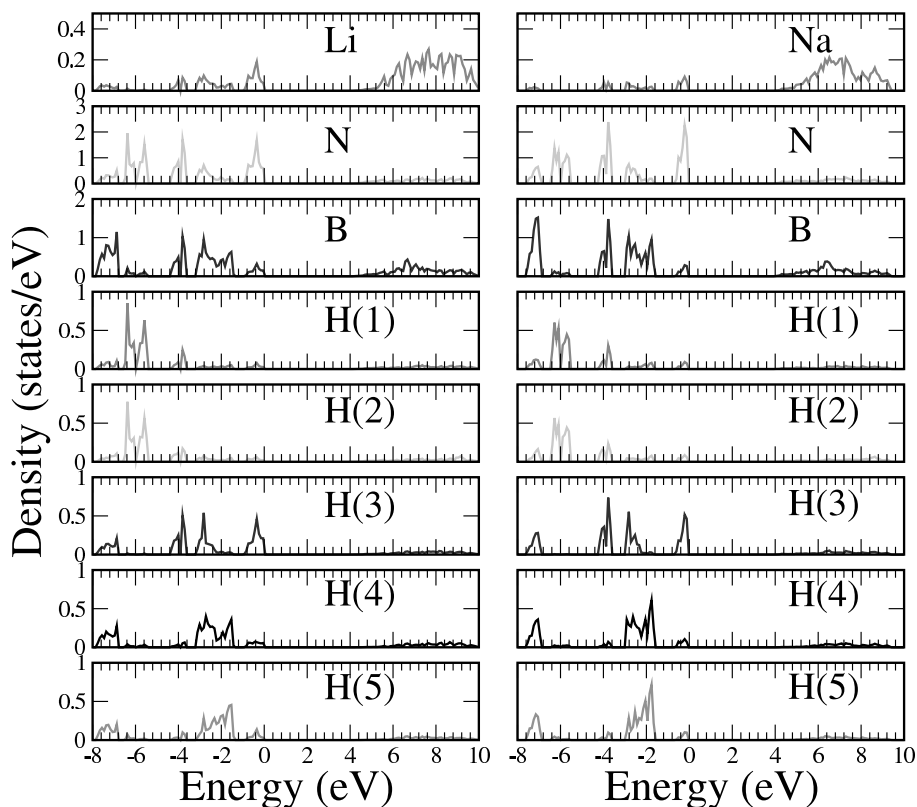


Figure 7.2. The total (first row) and partial (second to last rows) densities of states for  $\text{LiNH}_2\text{BH}_3$  (left column) and  $\text{NaNH}_2\text{BH}_3$  (right column). The Fermi level coincides with 0 eV.

found the hydrogen release taking place in the same temperature range (90-110 °C) for both  $\text{LiNH}_2\text{BH}_3$  and  $\text{NH}_3\text{BH}_3$ .

## 7.2 $\text{LiBH}_4 \cdot \text{NH}_3$ , $\text{Sr}(\text{NH}_2\text{BH}_3)_2$ and $\text{Li}_2\text{Al}(\text{BH}_4)_5 \cdot 6\text{NH}_3$

Three new compounds have been synthesized to study their performance for hydrogen storage  $\text{LiBH}_4 \cdot \text{NH}_3$  [34],  $\text{Sr}(\text{NH}_2\text{BH}_3)_2$  [35], and  $\text{Li}_2\text{Al}(\text{BH}_4)_5 \cdot 6\text{NH}_3$  [36]. The idea in paper VI is to make a theoretical study in detail of their electronic structures and to analyze the energetics of the hydrogen desorption.

atom	number of electrons
Li	0.13
B	1.44
N	6.20
H1	1.59
H2	0.60
H3	0.59
H4	1.63
H5	1.58

**Table 7.2.** Calculated Bader atomic charges (in number of electrons) for  $\text{LiBH}_4\text{NH}_3$  in the  $Pnma$  structure. Concerning the hydrogen atoms, we have used the same labeling as in the experimental paper (only inequivalent atoms are shown): H2 and H3 are bonded with N, while H1, H4, and H5 are bonded with B.

### 7.2.1 $\text{LiBH}_4 \cdot \text{NH}_3$

The two most relevant bonds in  $\text{LiB}_3 \cdot \text{NH}_4$  are the  $\text{N-Li}^+$  bond, which control the release of  $\text{NH}_3$  upon heating, and the  $\text{N-H} \cdots \text{H-B}$  bond which is the key for the dehydrogenation process. In Table 7.2 the calculated charge distribution in  $\text{LiBH}_4 \cdot \text{NH}_3$  is presented. We can see that lithium is almost fully ionized, with only 0.13 electrons remaining in the corresponding Bader basin, while  $\text{BH}_4$  carries a charge of -0.87. The ammonia molecule ( $\text{NH}_3$ ) is neutral, with eight electrons in total.

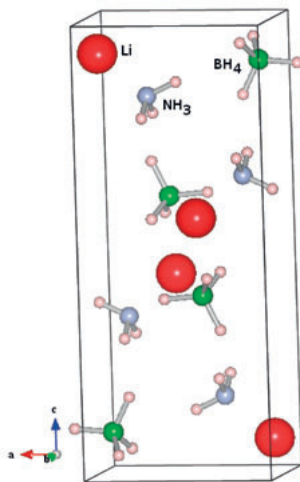


**Figure 7.3.** Crystal structure of  $\text{LiBH}_4 \cdot \text{NH}_3$  as obtained from our ab initio calculations.

We also analyzed the electron distribution by looking at the electron density in a plane. In Fig. 7.4, we can see our calculated electron density in the plane of the B, Li, and N atoms. The electron distribution between  $\text{Li}^+$  and the neighboring atoms is very low, which confirms that the bonding is mainly ionic, although an electron density can



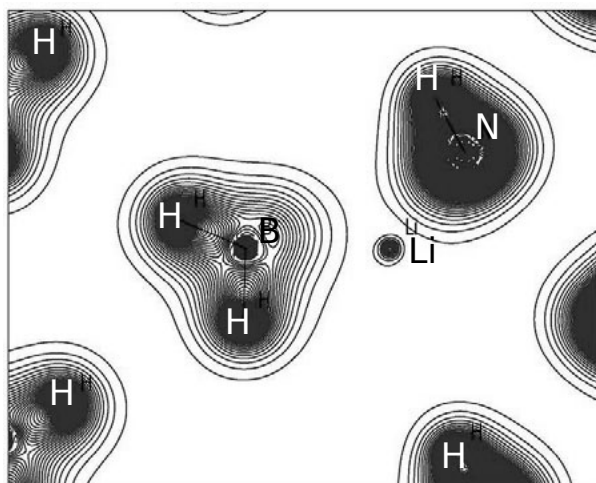


Figure 7.4. Calculated electron density of  $\text{LiBH}_4 \cdot \text{NH}_3$  in the plane of B-Li-N. The contours are  $0.05 \text{ e}/\text{\AA}^3$ .

remain in between the atoms provided that it is below the resolution that we have used for the plots.

Our calculated total and partial densities of states are presented in Fig. 7.5. It is clear that the compound is an insulator with a band-gap of more than 5 eV. The total DOS is made of four well-separated regions in energy: the first one is simply a peak around -15 eV, and it corresponds to the N-2s states. In PDOS we can see that there is a small contribution of Li at the same energy, which indicates that the bonding is not totally ionic, but contains also a small part of covalency. The second region corresponds to states between -8 eV and -4 eV. It is made of several peaks coming from N-p and B-s states, together with a contribution from lithium. As for the peak around -15 eV, this contribution from lithium is probably induced by a residual covalent bond with the neighboring atoms. Then from -3 eV to 0 eV there are mainly B-p states with N-p and Li states. Finally, the fourth region above the Fermi level (which is put at 0 eV) is made of conduction bands: the bottom of the conduction band is constituted from B-states with smaller contribution from Li and N.

### 7.2.2 $\text{Sr}(\text{NH}_2\text{BH}_3)_2$

Strontium amidoborane  $\text{Sr}(\text{NH}_2\text{BH}_3)_2$  begins to decompose to  $\text{Sr}(\text{NBH})_2$  and  $\text{H}_2$  at 60 °C. In addition,  $\text{Sr}(\text{NBH})_2$  continue to decompose releasing large amount of  $\text{NH}_3$  and small amounts of  $\text{B}_2\text{H}_6$ . The optimized structure was obtained by the same procedure as above (see Fig. 7.6). Our calculated Sr-N bond length of 2.58 Å is shorter than the experimental value of 2.68 Å, but our calculated B-N bond length of 1.54 Å, agrees very well with that given by Zhang et al. of 1.53 Å.

The Bader charges in Table 7.3 show that strontium is ionized to  $\text{Sr}^{1.58+}$  (if it had been fully ionized it would have a charge of +2). The  $\text{NH}_2$  have a charge of -0.90 and  $\text{BH}_3$  has a charge of +0.11. The electron density in plane Sr-N-H is shown in Fig. 7.7

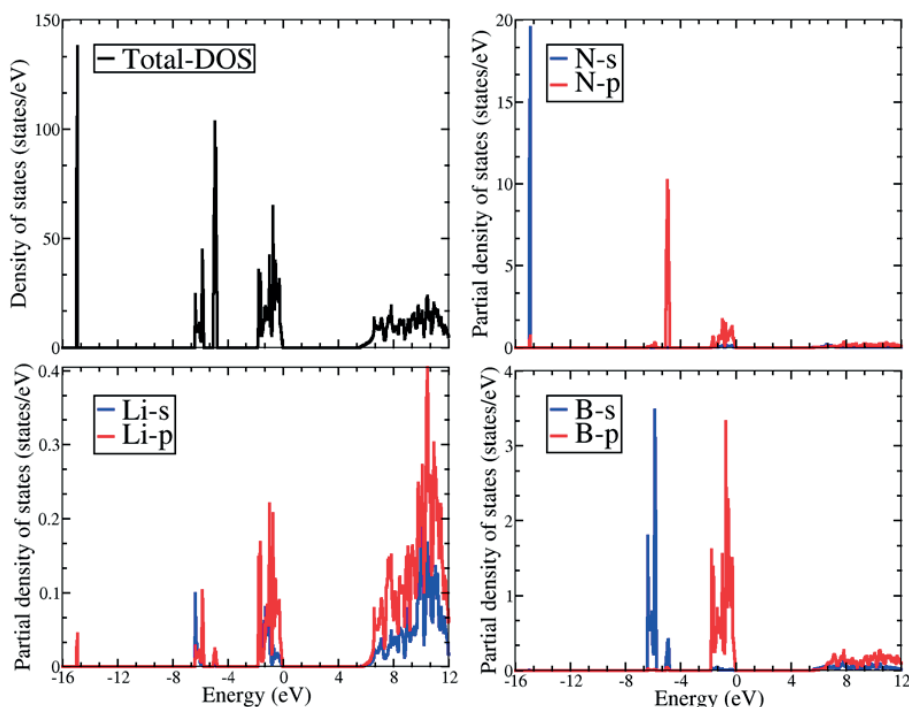


Figure 7.5. The total and partial densities of states for  $\text{LiBH}_4\cdot\text{NH}_3$ .

and we can see a region of low electron density, an indication of a mainly ionic bond. The total and partial DOS are shown in Fig. 7.8. The calculated band-gap is 4 eV. We have a first region at -16 eV made up of Sr-p states and N-s states, which implies a part of covalency in a mainly ionic bond. The region between -6 eV and 0 eV corresponds to a mix of N-p, B-s and B-p states. Finally there is a conduction band made up of Sr, N and B p-states.

The electron density in the plane of Sr-N-H is shown in Figure 7.7, and we can see a region of low electron density surrounding the Sr atom, an indication of a mainly ionic bond. However, this picture is obscured in this plot by the fact that Sr-4s and Sr-4p states have been included as valence electrons in our calculations.

The total and partial DOS are shown in Figure 7.8. The Sr-p states and N-s states constitute a region at -16 eV that implies a part of covalency in a mainly ionic bond. Our calculated hydrogen removal energies are 5.04 eV for the B-site and 5.54 eV for the N-site. It is instructive to compare these values with the ones obtained for  $\text{LiNH}_2\text{BH}_3$ . In this case, the values are 5.63 eV for the B-site and 6.02 eV for the N-site. Therefore, the B-H and N-H are weaker in  $\text{Sr}(\text{NH}_2\text{BH}_3)_2$  than in  $\text{LiNH}_2\text{BH}_3$ , which is favorable for the formation of  $\text{H}_2$ , although the replacement of lithium by strontium is not favorable in terms of the percentage of H in the total weight.

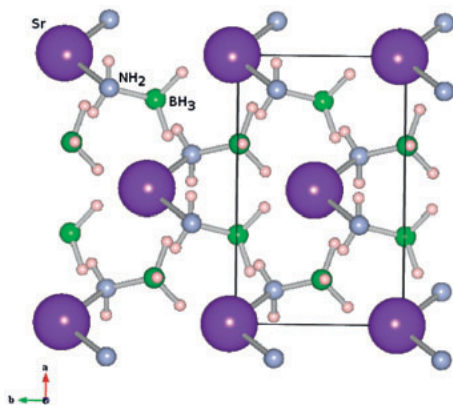


Figure 7.6. Crystal structure of  $\text{Sr}(\text{NH}_2\text{BH}_3)_2$  as obtained from our ab initio calculations. Here, Sr is shown in purple, N is grey, B is green and H in beige.

atom	number of electrons
Sr	8.4187
N	6.6620
B	0.0470
H(1)	0.6197
H(2)	0.6553
H(3)	1.9461
H(4)	1.9460

**Table 7.3.** Calculated Bader atomic charges (in number of electrons) for  $\text{Sr}(\text{NH}_2\text{BH}_3)_2$  in the monoclinic structure.

### 7.2.3 $\text{Li}_2\text{Al}(\text{BH}_4)_5 \cdot 6\text{NH}_3$

$\text{Li}_2\text{Al}(\text{BH}_4)_5 \cdot 6\text{NH}_3$  is a double-cation ammine borohydride, which was recently synthesized and studied by Guo et al. [36] using thermogravimetry and mass spectroscopy. They found >10 wt % of hydrogen release below 120 °C, leading toward a promising path to the chemical control of the dehydrogenation properties of the ammine borohydrides. The Al-N and Li-B bonds in  $\text{Li}_2\text{Al}(\text{BH}_4)_5 \cdot 6\text{NH}_3$  are very important to understand the electronic structure. We have reproduced very well the Al-N bond length, which was found experimentally [36] to be 2.05 Å. After having resolved the crystal structure of  $\text{Li}_2\text{Al}(\text{BH}_4)_5 \cdot 6\text{NH}_3$ , we focus on the electronic properties of this material. From the Table 7.4, it is clear that the  $\text{BH}_4$  molecules are mostly ionic in nature, having charges of -0.86 (with  $\text{BH}_4$  consisting of B<sub>2</sub>, H<sub>4</sub> and H<sub>5</sub>) and -0.72 (with  $\text{BH}_4$  consisting of B(1), H(6), and H(7), respectively, instead of -1, whereas ( $\text{NH}_3$ ) molecule is neutral, keeping eight electrons. Moreover, lithium and aluminum are partially ionized, with 0.11 and 0.57 electrons remaining, respectively. Our calculated electron densities in the planes of the N, Al, and H atoms and Li, B, and H atoms are shown in Figures 7.10 and 7.11, respectively. A very low distribution of electrons between  $\text{Al}^+$  and the neighboring atoms, as presented in Figure 7.10, supports our findings that the bonding is mainly ionic between these atoms. The electron

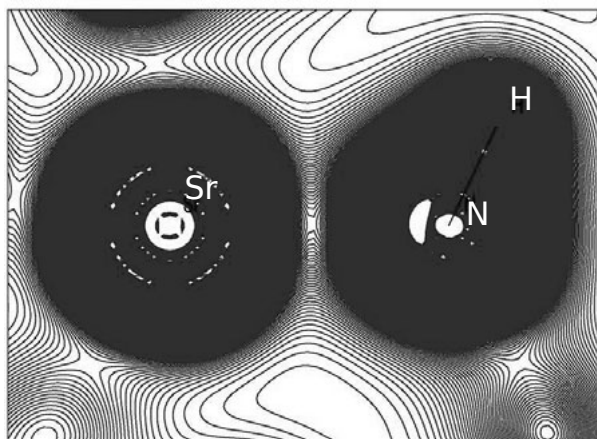


Figure 7.7. Calculated electron density of  $\text{Sr}(\text{NH}_2\text{BH}_3)_2$  in the plane of Sr-N-H. The contours are  $0.05 \text{ e}/\text{\AA}^3$ .

distribution between  $\text{Li}^+$  and the neighboring atoms is negligible, which confirms that the bonding is ionic. (See Fig. 7.11.)

We present in Figure 7.12 the calculated DOS of  $\text{Li}_2\text{Al}(\text{BH}_4)_5 \cdot 6\text{NH}_3$ . In the total DOS we can see a peak is around -16 eV that mainly consists of N-2s states with a small contribution of Al-p states, which shows that the nature of Al bonding with N is not fully ionic, but it also contains a small part of covalent bonding. Around -7 to -5 eV there are several peaks coming from N-p and B-s states, together with a contribution from aluminum, revealing the presence of covalent nature of bonding between Al with B and N bonds. Finally, the region above the Fermi level (which is put at 0 eV) is made of conduction bands: the bottom of the conduction band is constituted from B-p, N-p, and lithium states with a small contribution from aluminum.

We study the binding strength of hydrogen at the B and N sites by calculating the hydrogen removal energy. We find that the hydrogen removal energies are 5.32 vs. 5.38 eV for N and B-sites, respectively. This is in contrast with our results for  $\text{LiBH}_4 \cdot \text{NH}_3$  and  $\text{Sr}(\text{NH}_2\text{BH}_3)_2$ , for which the N-H bond was stronger than the B-H bond.

### 7.3 Molecular dynamic simulations

We have also looked at the mobility of the hydrogen species. To have a comparison, we conducted our simulation for the same period of time (5 ps) and for the same temperature (500 K) for all three materials. Our results of the mean square displacements (MSDs) are presented in Fig. 7.13 - 7.14. We observe that the diffusion of hydrogen in  $\text{LiBH}_4 \cdot \text{NH}_3$  appears to be faster than that in  $\text{Sr}(\text{NH}_2\text{BH}_3)_2$  and  $\text{Li}_2\text{Al}(\text{BH}_4)_5 \cdot 6\text{NH}_3$  because at the end of our simulation the MSD of hydrogens in  $\text{LiBH}_4 \cdot \text{NH}_3$  is clearly larger (close to  $100 \text{ \AA}^2$  at 5 ps) than the corresponding MSD in  $\text{Sr}(\text{NH}_2\text{BH}_3)_2$  and  $\text{Li}_2\text{Al}(\text{BH}_4)_5 \cdot 6\text{NH}_3$  (between 10 and  $20 \text{ \AA}^2$  at 5 ps). This is partially explained by the fact that the crystal structures are different: geometries that are less compact

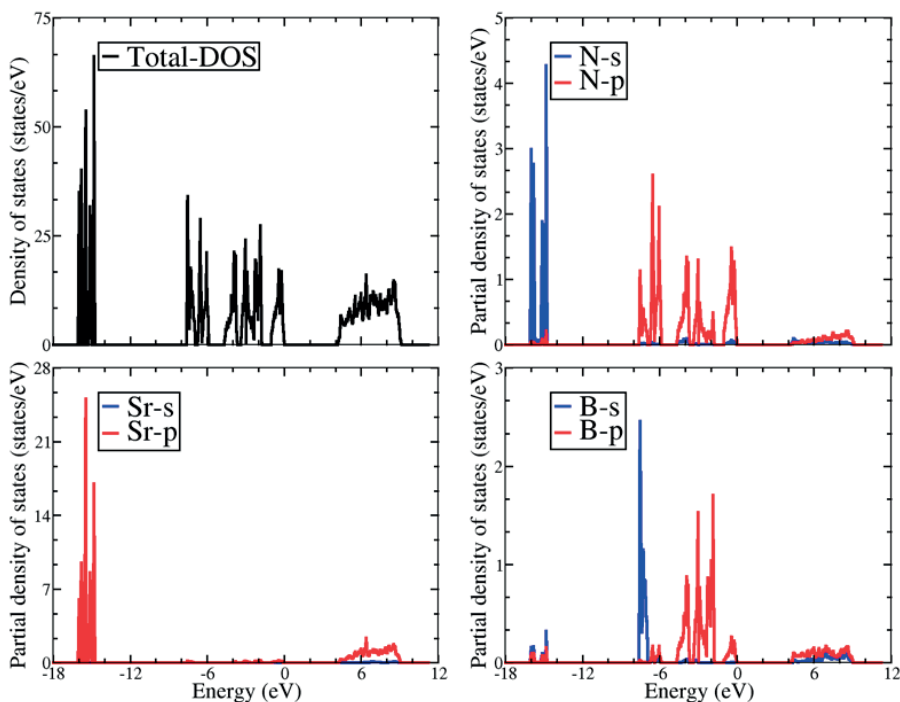


Figure 7.8. The total and partial densities of states for  $\text{Sr}(\text{NH}_2\text{BH}_3)_2$ .

are more favorable for hydrogen transport. Also, as shown by our calculations of the hydrogen removal energies, the environment of the hydrogen atoms is different, and this can play a role on the MSD values, especially at the beginning of the simulations when the hydrogen atoms are still located close to their equilibrium position.

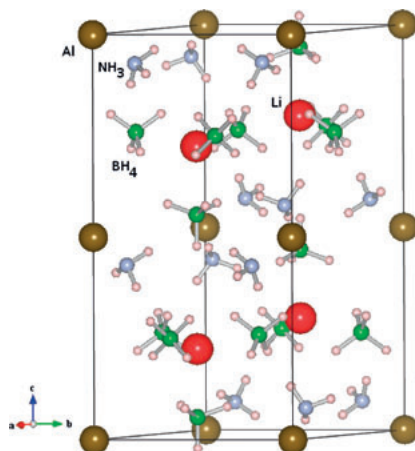


Figure 7.9. Crystal structure of  $\text{Li}_2\text{Al}(\text{BH}_4)_5 \cdot 6\text{NH}_3$  as obtained from our ab initio calculations.

atom	number of electrons
Li	0.0116
Al	0.0759
N	6.4264
B(1)	0.0481
B(2)	0.0483
H(1)	0.5516
H(2)	0.5541
H(3)	0.5545
H(4)	1.9765
H(5)	1.9559
H(6)	1.9248
H(7)	1.9508

**Table 7.4.** Calculated Bader atomic charges (in number of electrons) for  $\text{Li}_2\text{Al}(\text{BH}_4)_5 \cdot 6\text{NH}_3$ .

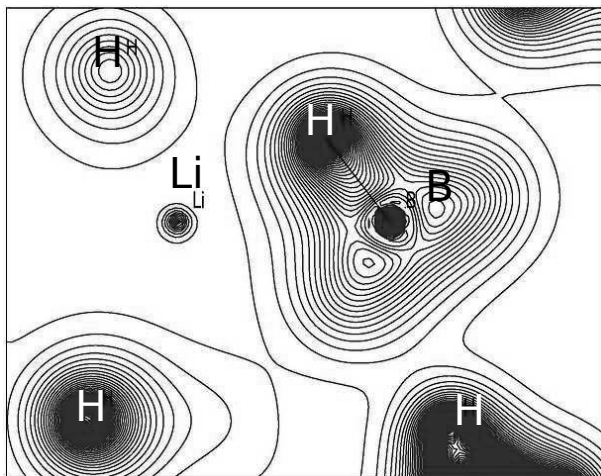


Figure 7.10. Calculated electron density of  $\text{LiBH}_4 \cdot \text{NH}_3$  in the plane of Li-B-H. The contours are  $0.05 \text{ e}/\text{\AA}^3$ .

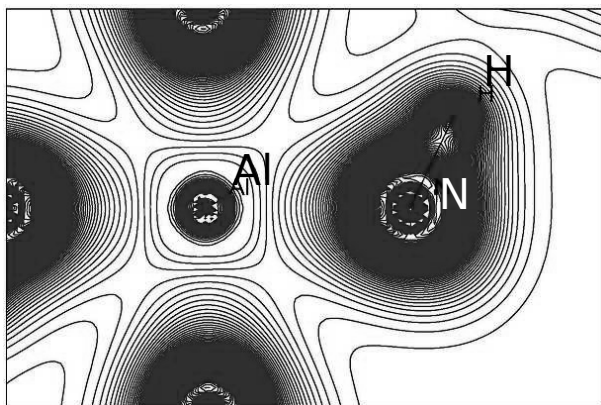


Figure 7.11. Calculated electron density of  $\text{Li}_2\text{Al}(\text{BH}_4)_5 \cdot 6\text{NH}_3$  in the plane of Al-N-H. The contours are  $0.05 \text{ e}/\text{\AA}^3$ .

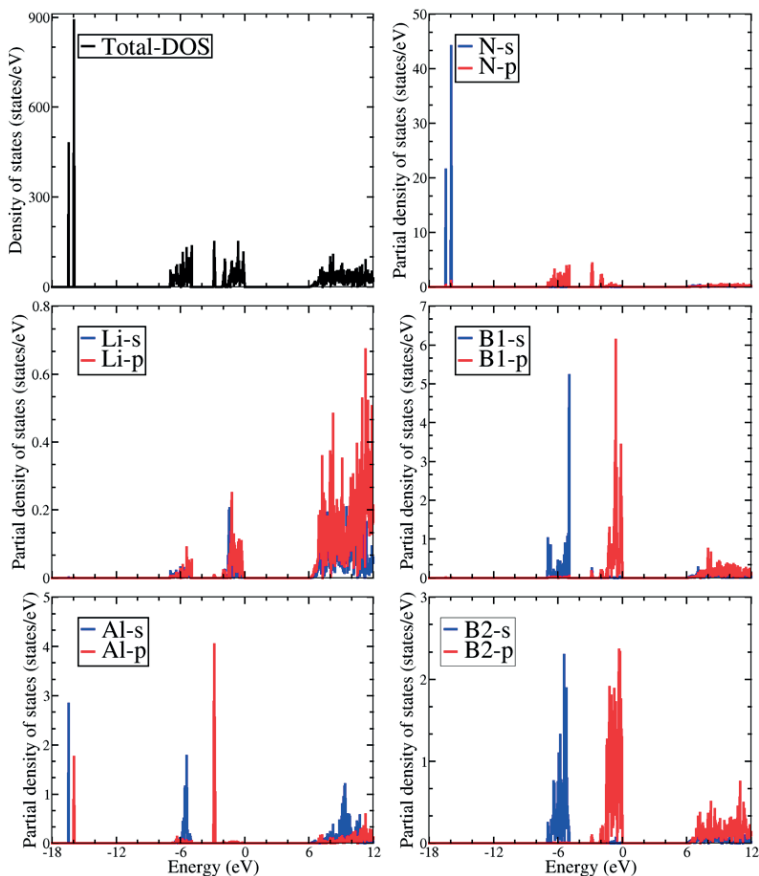


Figure 7.12. The total and partial densities of states for  $\text{LiBH}_4 \cdot \text{NH}_3$ .

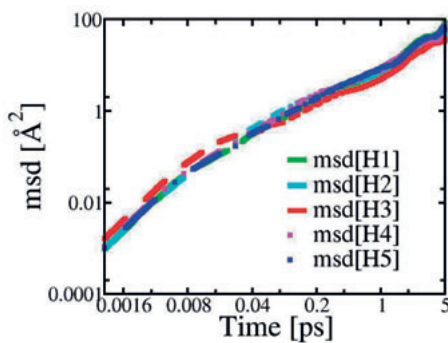


Figure 7.13. Diffusion of hydrogen atoms in  $\text{LiBH}_4 \cdot \text{NH}_3$ .



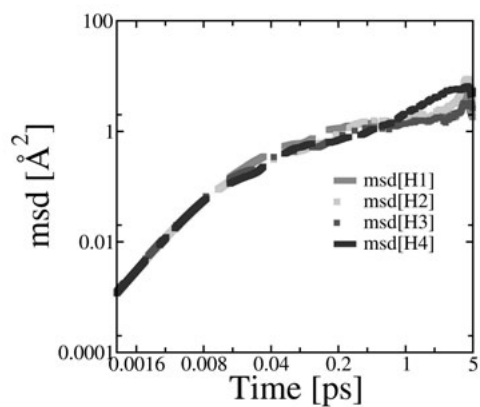


Figure 7.14. Diffusion of hydrogen atoms in  $\text{Sr}(\text{NH}_2\text{NH}_3)_2$ .

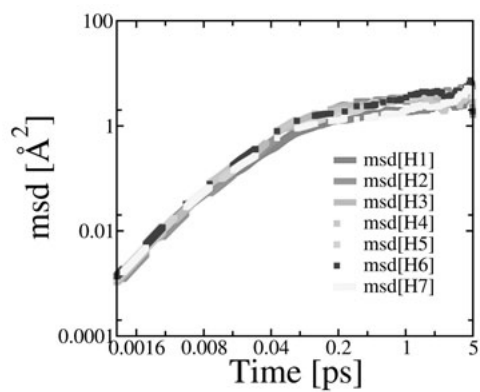


Figure 7.15. Diffusion of hydrogen atoms in  $\text{Li}_2\text{Al}(\text{BH}_4)_5 \cdot 6\text{NH}_3$ .

## 8. Chemical Vapor Deposition Grown $\alpha$ -Al<sub>2</sub>O<sub>3</sub>

Alumina (Al<sub>2</sub>O<sub>3</sub>) is an important material used in many technological applications and one such application that is of particular interest here is as protective coating material for cutting tools. In paper V and VII we are investigating the catalytic mechanism of H<sub>2</sub>S and possible point defect formations in the growth process, respectively.

### 8.1 The Catalytic Mechanism of H<sub>2</sub>S

The catalytic effect of H<sub>2</sub>S in chemical vapor deposition (CVD) growth of  $\alpha$ -Al<sub>2</sub>O<sub>3</sub> is not very well known and have only been studied a few times before [37, 38]. There are also a few studies about H<sub>2</sub>S adsorption [39] - [42] but they do not consider other species present in the CVD-reaction. We use a number of different theoretical tools such as the Calphad approach, DFT, molecule dynamics (MD) and Nudge Elastic Band Method (NEB) to clarify the role that H<sub>2</sub>S has on the gas phase thermodynamics and surface kinetics of  $\alpha$ -Al<sub>2</sub>O<sub>3</sub>.

#### 8.1.1 AlO- and AlO:Cl-surface

Since Cl act as an Lewis base because of its high electronegativity we choose it as an terminating species for the AlO-surface. We did not consider hydrogen, that is also abundant in the CVD gas chamber, as a terminating species because previous works indicate that H stabilizes the O-surface.

#### AlAl- and AlAl:Cl surface

We have seen from MD-simulations that atoms from the second layer diffuse down to empty bulk positions in the 4th layer below oxygen. The reason seems to be that the AlAl-surface is the most unstable surface at the CVD temperature of 1283 K.

The AlO- and AlAl-surface is thermodynamically and dynamically stabilized (see Table 8.1) as it is terminated by chlorine. The surfaces undergo considerably less reconstruction if it is chlorinated.

#### O- and O:H surface

In Fig. 8.3 display the [1110]-direction of the O-surface, showing that the top layer of oxygen rotated considerably around the symmetry axis, and thus distorted heavily from their ideal Wyckoff positions (Fig. 8.3(c) compared to 8.3(b)). We believe that this rotation could be a sign of destabilization of the bare O-surface. Based on previous work we choose to H-terminate the O-surface and we also tried with and without fixing

Surface	Termination	$\Delta E$ (eV/atom)	$\Delta E$ (kJ/mol)
AlO)	1Cl	-0.38	-37
AlO)	4Cl	-0.52	-51
AlAl	4Cl	-3.68	-355
AlAl	8Cl	-2.55	-246
O	12H	-2.70	-260

**Table 8.1.** Heat of formation at 0K compared with experimental data.

the 6 bottom layers. The agreement with previous DFT-results is much better than for the bare O-surface. In Fig. 8.3(d) we can see the H-atoms lock the O-atoms to their ideal positions, and thereby stabilize this surface, enabling continuous growth of the [1110]-direction .

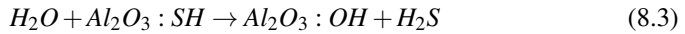
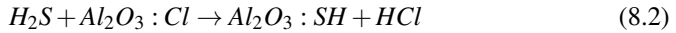
### 8.1.2 Surface reactions

It is very difficult to determine the exact growth mechanism since the possible number of reactions at the surface in CVD are countless and also there is a difficulty in determining the exact order in which molecules in gas phase form new layers. However, one can make an educated guess of possible surface reactions.

One such pathway could be



The reaction barrier for this process is rather large, namely 3.00 eV. An alternate pathway of hydroxylating the Al-surface, might be by the use of  $H_2S$  as an intermediate in a two step reaction,



which results in reduced barrier heights, 1.42 eV for the first part of the reaction and 1.95 eV for the second part. Slager et al. [42] studied the adsorption of  $H_2S$  onto  $Al_2O_3$ , where they suggested a mechanism, consistent with their measured data, where  $H_2S$  is adsorbed to an exposed  $Al^+$ -ion forming an Al-S surface bond and H-bonding to neighboring OH-species. Our results may also support these observations, since the adsorption mechanism of  $H_2S$  which we suggest from these data includes the formation of AlS bonds.

The relative increase in reaction rate is about 5 orders of magnitude for the first  $H_2S$  reaction compared to the reaction of  $H_2O$ , and of about 4 orders of magnitude for the second reaction where  $H_2S$  again is formed. This qualitative estimation leads to the conclusion that  $H_2S$  is kinetically preferred before  $H_2O$  under the considered conditions.

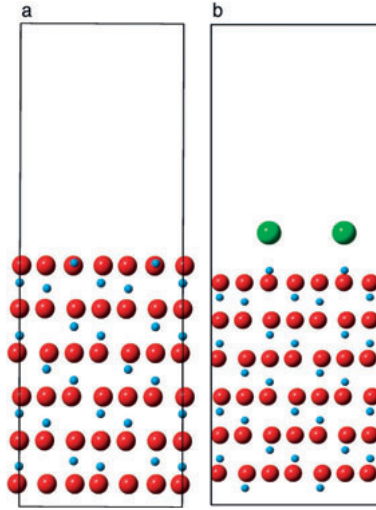


Figure 8.1. Side view of (a) AlO-surface geometry after relaxation. (b) Chlorated AlO-surface after MD-simulation. Al-small black balls, O-large red balls, Cl-largest green balls.

## 8.2 Possible Point Defects

In paper VII we investigate possible incorporation of intrinsic and extrinsic defects into CVD-grown  $\alpha$ - $\text{Al}_2\text{O}_3$ . The possible extrinsic defects which are present in the reactor from the precursor species are C, H, Cl and S. We compare the defect formation energies from reference states and look for compensating charge defects.

In Fig. 8.4, the heat of formation of all the investigated intrinsic and extrinsic defects calculated at the three different experimental conditions are displayed. Some of the defects are dependent on the oxygen gas pressure. These defects are the aluminum interstitial,  $\text{Al}_I$ , the aluminum vacancy,  $\text{V}_{\text{Al}}$ , the oxygen vacancy,  $\text{V}_\text{O}$ , the oxygen interstitial,  $\text{O}_I$ , and the impurities replacing oxygen which we denote as  $\text{Cl}_\text{O}$  (chlorine),  $\text{S}_\text{O}$  (sulfur),  $\text{C}_\text{O}$  (carbon) and  $\text{H}_\text{O}$  (hydrogen). The interstitial impurities  $\text{Cl}_I$  (chlorine),  $\text{S}_I$  (sulfur),  $\text{C}_I$  (carbon) and  $\text{H}_I$  (hydrogen) are approximated as independent of oxygen pressure since they do not replace the oxygen in the lattice and thus the heat of formation are the same under all conditions. They are however indirectly dependent since they are formed from oxygen containing species.

One can from Fig. 8.4 conclude that the heat of formation from the simulated CVD gas phase lies in between the extreme conditions of high and low oxygen gas pressure. We can also see that the trends are, for both dopants and intrinsic defects, independent of reference states. This reassures us that our method of calculating both solids and molecules within the DFT approach gives qualitatively reasonable results. We can also see that the neutral defects  $\text{H}_I$  and  $\text{C}_I$  have the lowest formation energies at CVD condition.

Furthermore we found that carbon interstitial  $\text{C}_I$  has amphoteric properties (see Fig. 8.5) as do also  $\text{H}_I$ ,  $\text{H}_\text{O}$  and  $\text{S}_I$ .

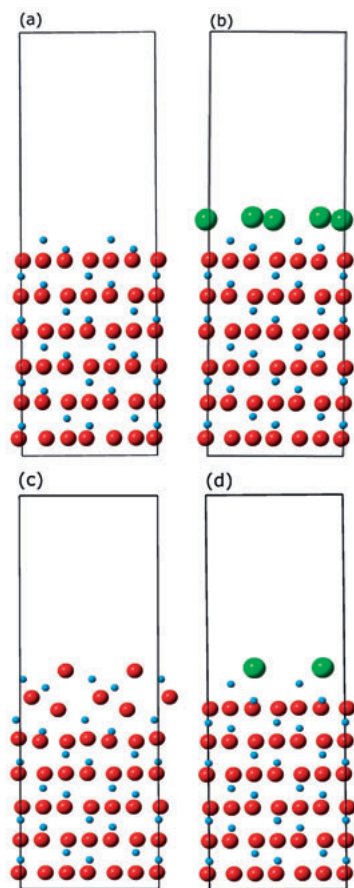


*Figure 8.2.* AlAl-surface after geometry relaxation, before MD. (b) Chlorated AlAl-surface (Cl on both exposed Al-layers) after MD. (c) AlAl-surface after MD. (d) Chlorated AlAl-surface (Cl only on the top Al-layer). Al small blue balls, O large red balls, Cl green balls.

It seems from the formation energy data that inclusion of extrinsic defects, even if they are charge compensated, do not form. This provides some explanation to why CVD grown  $\alpha$ -Al<sub>2</sub>O<sub>3</sub> is of high quality.

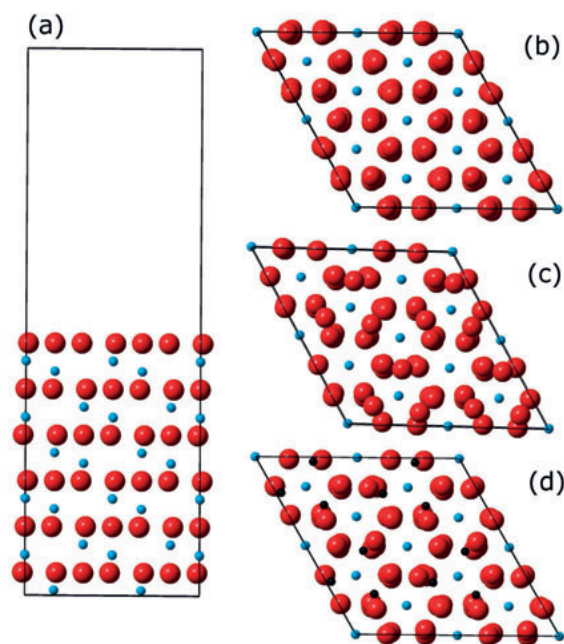


Figure 8.3. O-surface of an  $\text{Al}_2\text{O}_3$  slab before geometry relaxation, (a) side view and (b) top view. Geometry optimization of (c) the pure O surface and (d) H terminated O surface. Al blue small balls, O red large balls, H black small balls.

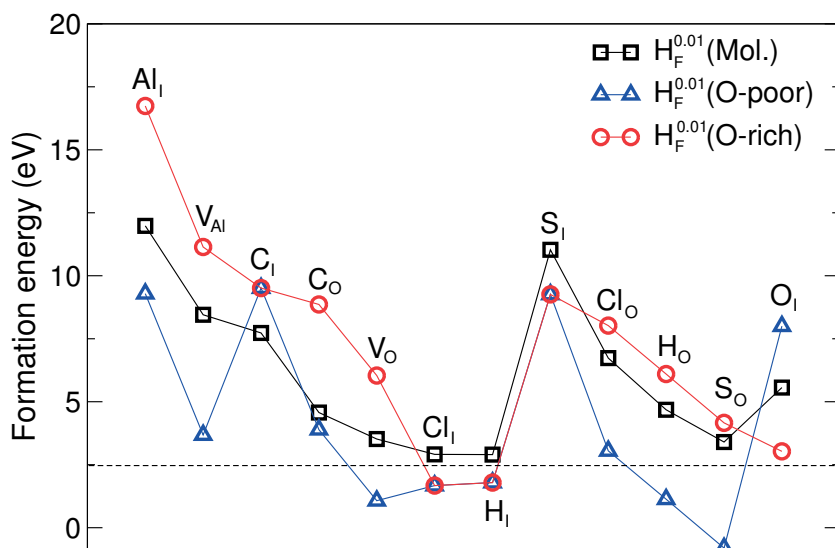


Figure 8.4. The formation energies of the neutral intrinsic defects and extrinsic impurities at a concentration of 1.24 (substitutional) and 1.25 at% respectively.

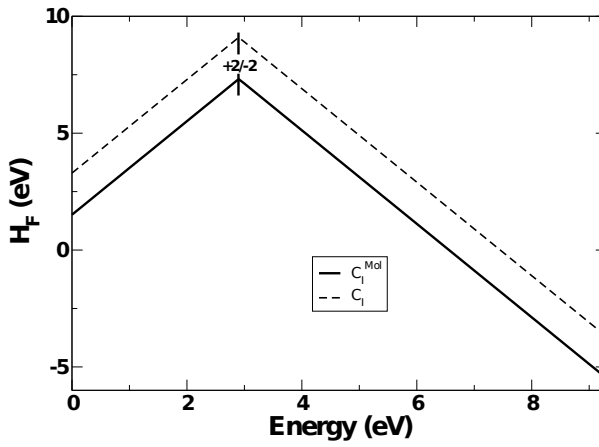


Figure 8.5. The heat of formation as a function of Fermi energy for the carbon interstitial. Two experimental conditions are displayed.  $H_F^{Mol}$  and  $H_F^{SER}$  (the latter is without notation).

## 9. Conclusions and Outlook

Despite years of intense research efforts the question remains unanswered: Is it possible to realize room temperature dilute magnetic semiconductors? We have studied two different types of doped TM-oxides in an attempt to come closer to the answer. It is well known that local density approximation (LDA) often underestimates the band gap. Consequently it is likely that defect levels from impurities also could be incorrect with respect to the host band. An improvement to some of the problems in LDA is LDA+U. A calculation with LDA+U was done on co-doped (Mn,Al)-ZnO to see if it could shed some light on the problem of theoretical and experimental discrepancy. The result could however not provide any explanation for the reported increase in magnetic moment. In the future, a study with more advanced methods such as dynamical mean field theory (DMFT) or the ferromagnetic Kondo-lattice model compared with angle and spin resolved photoemission experiments may provide additional insights. It is not only the theoretical models that can be insufficient. A correct theoretical description of a real system measured upon is also desirable if an adequate comparison between experimental data and theoretical results is to be made. In the view of this we have studied influence of defects on ferromagnetism and their formation energies. There seems to be a significant discrepancy between the reported experimental findings. Sometimes this has to do with different growth techniques and on other times due to the sensitivity of different experimental probing techniques and interpretation thereof. Up to now to our knowledge, there is no way of experimentally determining the exact distribution of magnetic ions, defects or various distortions. This, however, could be just a question of time before better techniques being developed.

Ammonia borane and similar compounds are attractive as hydrogen storage materials but are held back by some shortcomings such as unclean hydrogen release and polymerization which makes regeneration of the materials difficult. In an attempt to improve the properties, addition of light-weight metals has been investigated. Our results are in line with experimental findings and we hope that the gained understanding will inspire further experimental studies of these compounds.

Finally, we have suggested a catalytic mechanism for  $\text{H}_2\text{S}$  in the CVD growth process of  $\text{Al}_2\text{O}_3$ , a probable candidate for termination of the AlO-surfaces and a probable transition state molecule. It is of great importance that these theoretical findings are followed up by experimental studies and by the examination through further refined theoretical models and methods. For instance, molecules formed at low concentrations,  $\leq 10^{-3}$  mole fraction, should be considered. The kinetics on the surface should be studied by nudge elastic band method or comparable methods. Also a comparative study between different polymorph would be desirable.



# Summary in Swedish

Denna avhandling handlar om funktionella material för tre olika tekniska områden, spintronik, väteagring, skärverktyg.

Spintronik är ett nytt forskningsområde som kombinerar magnetism och elektronik. Det grundläggande konceptet för spintronik är manipulering av spin, till skillnad från vanlig elektronik där elektron spinnet ignoreras och endast laddningen hos elektronen används. Jämfört med befintlig mikroelektronik, ger möjligheten att kontrollera och manipulera både laddning och spinn med hjälp av externa elektriska och magnetiska fält utökade förmågor och möjliggör en vidare miniaturisering. Artikel III behandlar zinkoxid (ZnO) co-dopade med magnesium och aluminium. Tanken med dopning är att införa ett magnetiskt moment i en halvledare genom att delvis ersätta en del kationer (Zn i detta fall) med en övergångsmetall (Eng. Transition metal, TM) (Mn). Denna typ av halvledarmaterial kallas utspädd magnetisk halvledare (eng. diluted magnetic semiconductors, DMS). ZnO-baserade material har fått stor uppmärksamhet på grund av specifika elektriska, optiska och akustiska egenskaper, som har många praktiska applikationer såsom lysdioder, laserdioder och detektorer för UV-våglängdsområdet. Därför har stora ansträngningar gjorts för att syntetisera ZnO-baserade DMS material. Problemet är att experimentella mätningar på ZnO-baserade DMS material givit motstridiga resultat. Till exempel har Co-ZnO, Ni-ZnO, och Mn-ZnO funnits vara paramagnetiska, medan andra rapporterar ferromagnetism i Co-ZnO och Mn-ZnO både i bulk och i tunn film. Flera aktuella studier på Mn-ZnO har visat att ferromagnetism är starkt beroende av vilken metod som används och under vilka villkor som framställningen av provet skett under. Magnetismen i ZnO-baserade DMS verkar vara känsliga för den kemiska ordningen av magnetiska joner och defekter som vakanser och interstitialer. Spintronik kräver att ferromagnetism är inneboende., dvs inte från magnetiska TM kluster eller fasorenheter. En grundläggande förståelse av magnetiska egenskaper och nanostrukturer av ZnO DMSs är avgörande för utvecklingen av spintronikapparater.

Dessutom har ferromagnetism med hög Curie-temperatur och stor nettomagnetiskt moment observerats i många halvledare utan tillsats av TM joner. I artiklarna I och IV avhandlas ett välkänt sådant material  $\text{In}_2\text{O}_3$ , i fråga om olika inneboende defekters inflytande på ferromagnetism. Enligt våra teoretiska beräkningar uppvisar p-dopad, särskilt metall / kation vakansen, en stabil ferromagnetiska koppling.

Väteagringmaterial är en viktig del av en ny vätgasekonomi som förhoppningsvis ska ersätta dagens fossila bränslen som energibärare. Dagens energi- och transport ekonomi är främst beroende av fossila bränslen som kol, olja och naturgas. Mot bakgrund av dagens ökad medvetenheten om klimatförändringar och det så kallade "peak oil" scenariot, har ett sökande efter alternativ pågått under en längre tid. Alternativa tekniker och material har varit kända i årtionden, men har aldrig lyckats att konkurrera med konventionell teknik av olika skäl. Vätgas är en attraktiv energibärare eftersom den är förnybar och icke förorenande. Dock har problemet med att lagra vätgas på ett

säkert och effektivt sätt begränsat dess praktiska användning som bränsle för mobila applikationer.

Lagring av vätgas kan göras på flera olika sätt, t.ex. starkare material för behållare, sorbenter och hydrider. Mycket forskning har gjorts på material så som metallorganiska ramverk (MOF) eller silan ( $\text{SiH}_4$ ) och dess derivat ( $\text{SiH}_4 (\text{H}_2)_2$ ). Dessutom har lätta hydridmaterial rönt särskilt intresse eftersom de har bedömts vara de mest lovande material för att uppnå målet på hög gravimetrisk och volymetrisk lagringskapacitet. Särskilda ansträngningar läggs numera på bor-kväve-väte föreningar eftersom de erbjuder hög kapacitet för lagring av vätgas, tillsammans med rimliga dehydrogeneringsegenskaper. Artiklarna II och VI fokuserar på struktur och energiska egenskaper av metalladopade bor-kväve-väte föreningar.

Artiklarna V och VII diskuterar tillväxten av aluminiumoxid  $\text{Al}_2\text{O}_3$  i samband med kemisk förångningsdeposition (eng. chemical vapor deposition, CVD). I decennier har industrin använt CVD för tillverkning av slitstarka beläggningar på högpresterande hårdmetallverktyg. Bland de mer vanligt förekommande ytbeläggningsmaterialen är titankarbid och titannitrid  $\text{Ti}(\text{C},\text{N})$  och  $\text{Al}_2\text{O}_3$ . En attraktiv egenskap hos  $\text{Al}_2\text{O}_3$  är den kemiska stabiliteten vid hög temperatur och den relativt dåliga värmeledningsförmågan som ger ett mer effektivt termiskt skydd för substratet än  $\text{Ti}(\text{C},\text{N})$ . Denna egenskap möjliggör högre skärhastighet samtidigt som oönskad plastisk deformation av skärverktygets egg minimeras.

Så långt tillbaka som 1985 användes för första gången  $\text{H}_2\text{S}$  för att öka tillväxttakten av  $\text{Al}_2\text{O}_3$  och samtidigt åstadkomma en mer homogen tillväxt på flanker och kanterna av ett skärverktyg. Men den exakta mekanismen har inte varit känd även om en del undersökningar har gjorts. I artikel V drar vi slutsatsen från termodynamisk modellering och ab initio modellering att  $\text{H}_2\text{S}$  fungerar som en verklig katalysator för tillväxt av  $\text{Al}_2\text{O}_3$  ytan. Vi föreslår också en mekanism för den katalytiska mekanismen. Dessutom har det visat sig att AlO-ytorna termodynamiskt och dynamiskt stabiliseras om de termineras av klor eller, i fallet med syreytan, väte som finns i reaktorn. En annan fråga som avhandlas i artikel VII är defekter som skulle kunna bildas som en följd av CVD reaktionen. I CVD-reaktorn finns det många olika molekyltyper som kan bidra till att bilda punktdefekter såsom C, Cl, H och S. Hittills har våra beräkningar visat att det ej är energimässigt fördelaktigt att dessa typer av punkt defekter bildas. Det är i linje med experimentella mätningar som gett att CVD tillverkad  $\text{Al}_2\text{O}_3$  är av mycket ren natur, med det förbehållet att mycket små mängder av defekter är svåra att upptäcka.

# Acknowledgements

I would like to take the opportunity to thank my supervisor Rajeev Ahuja for the possibility to work at this excellent research group. A thank goes to Peter Larsson for all support and the fun conspiracy and philosophical discussions. Cecilia Århammar for her support, interesting and fun discussions and critical reading of this thesis. I would also like to thank Li Wen, Anders Bergman and Oscar Grånäs for reading parts of the thesis and share their opinions. I would like to thank Jonas Fransson for giving such interesting courses and all the help with understanding difficult problems. Thank you Ralph Sheicher for letting me boss you around and all the funny internet sites you sent me. Thanks, Wei Wei Sun for the beautiful hand fan you gave me, associated with the great strategist Zhuge Liang. A thank goes to the co-authors and collaborators in the projects: Lunmei, Sebastien, Andreia and Moyses. A big thanks goes to all the people at the Division of Materials Theory for making the staying here pleasant.

To all my friends, Tobbe, Daniel, Stefan, Tias, Peter, Anna, Björn, Gabriel, Göran, David, Henke, Maja, Ben, my favorite cuisine Kalle and to all my corridor friends past and present, thanks for all the fun and games we had over the years. And to Dominic, I hope we will make that magical trip one day.

And finally, I would like to express my warm gratitude to my family, Anders, Lena, Anna, Katarina, Per, Viktor, Klara, Göran and Maj-Britt for all their support.

# References

- [1] P.W. Atkins, R.S. Friedman, *Molecular Quantum Mechanics*, Third Edition, Oxford University Press (1997)
- [2] A Sazbo, N.S. Ostlund, *Modern Quantum Chemistry*, First Edition, Revised, McGraw-Hill Publishing Company (1989)
- [3] W. Heisenberg, *Zeitschrift für Physik*, 33, 879-893 (1925). English translation in: B. L. van der Waerden, *Sources of Quantum Mechanics* (Dover Publications, 1968) (English title: *Quantum Theoretical Reinterpretation of Kinematic and Mechanical Relations*).
- [4] P. M. A. Dirac. *Proceedings of the Royal Society of London A*, 114, 243 (1927)
- [5] J. Hubbard, *Proc. R. Soc. London, Ser A*, 276, 283 (1963)
- [6] J. Hubbard, *Proc. R. Soc. London, Ser A*, 281, 401 (1964)
- [7] A.I. Liechtenstein, V. I Anisimov, and J. Zaanen, *Phys. Rev. B*, 52, R5467 (1995)
- [8] V. I. Anisimov, F. Aryasetiawan and A. I. Lichtenstein, *J. Phys. Condens. Matter*, 9, 767 (1997)
- [9] Czyzyk and Sawatzky, *Phys. Rev. B*, 49, 14211 (1994)
- [10] B.R. Judd, *Operator Techniques in Atomic Spectroscopy*, McGraw-Hill, New York (1963)
- [11] D. C. Kundaliya, S. G. Ogale, S. E. Lofland, S. Dhar, C. J. Metting, S. R. Shinde, Z. Ma, B. Varughese, K. V. Ramanujachary, L. Salamanca-Riba, et al., *Nat. Mater.* 3, 709 (2005).
- [12] K. Sato and H. Katayama-Yoshida, *Phys. Status Solidi* 673 (2002).
- [13] N. A. Spaldin, *Phys. Rev. B* 69, 125201 (2004).
- [14] M. A. Garcia, M. L. Ruiz-Gonzalez, A. Quesada, J. L. Costa-Kramer, J. F. Fernandez, S. J. Khatib, A. Wennberg, A. C. Caballero, M. S. Martin-Gonzalez, M. Villegas, et al., *Phys. Rev. Lett.* p. 217206 (2005).
- [15] D. Iusan, B. Sanyal, and O. Eriksson, *Phys. Status Solidi* 204, 53 (2006).
- [16] A. L. Rosa and R. Ahuja, *J. Phys.: Condens. Matter* 19, 386232 (2007).
- [17] K. R. Kittilstved, N. S. Norberg, and D. R. Gamelin, *Phys. Rev. Lett.* (2006).
- [18] Q. Xu, H. Schmidt, L. Hartmann, H. Hochmuth, M. Lorenz, A. Setzer, P. Esquinazi, C. Meinecke, and M. Grundmann, *Appl. Phys. Lett.* 91, 092503 (2007).
- [19] X. H. Xu, H. J. Blythe, M. Z. A. J. Behan, J. R. Neal, A. Mokhtari, R. M. Ibrahim, A. M. Fox, and G. A. Gehring, *New J. Phys.* 8, 135 (2006).
- [20] T. Dietl, H. Ohno, F. Matsukura, J. Cibert and D. Ferrand, *Science*, 287 1019 (2000)
- [21] T. Dietl, *Semicond. Sci. Technol.* 17 377 (2002)
- [22] J. M. D. Coey, M. Venkatesan, and C. B. Fitzgerald, *Nature Mater.* 4 175 (2005)
- [23] L.M. Huang, C. Moysés Araújo and R. Ahuja, *EPL* 87 27013 (2009)
- [24] H.S. Hsu, et al., *Appl. Phys. Lett.* 88 242507 (2006)

- [25] J.E. Jaffe, T.C. Droubay, S.A. Chambers, J. Appl. Phys. 97 073908 (2005)
- [26] Z.G. Yu, et al., Phys. Rev. B 74 165321 (2006)
- [27] L. Bergqvist, et al., Phys. Rev. B 72 195210 (2005)
- [28] A. C. Stowe, W. J. Shaw, J. C. Linehan, B. Schmid, and T. Autrey, Phys. Chem. Chem. Phys. **9**, 1831 (2007).
- [29] M. G. Hu, R. A. Geanangel, and W.W. Wendlandt, Thermochim. Acta **23**, 249 (1978).
- [30] V. Sit, R. A. Geanangel, and W. W. Wendlandt, Thermochim. Acta **113**, 379 (1987).
- [31] G. Wolf, J. Baumann, F. Baitalow, and F. P. Hoffmann, Thermochim. Acta **343**, 19 (2000).
- [32] F. Baitalow, J. Baumann, G. Wolf, K. Jaenicke-Rößler, and G. Leitner, Thermochim. Acta **391**, 159 (2002).
- [33] Zhitao Xiong, Chaw Keong Yong, Guotao Wu, Ping Chen, Wendy Shaw, Abhi Karkamkar, Thomas Autrey, Martin Owen Jones, Simon R. Johnson, Peter P. Edwards, and William I. F. David, Nat. Mater. **7**, 138 (2008).
- [34] Y. Guo, G. Xia, Y. Zhu, L. Gao and X. Yu, Chem. Commun. **46**, 2599-2601 (2010).
- [35] Q. Zhang, C. Tang, C. Fang, F. Fang, D. Sun, L. Ouyang and M. Zhu, J. Phys. Chem. C **114**, 1709-1714 (2010).
- [36] Y. Guo, H. Wu, W. Zhou, and X. Yu, J. Am. Chem. Soc. **133**, 4690- 4693 (2011).
- [37] T. Oshika and A. Nishiyama and K. Nakaso and M. Shimada and K. Okuyama, J. Phys IV **9** 877 (1999).
- [38] T. Oshika and M. Sato and A. Nishiyama, J. Phys IV **12** 113 (2002).
- [39] Jean-Claude. Lavalley and Carl P. Tripp, J. Phys. Chem **90** 981-982 (1986).
- [40] C.R. Apesteguia and J.F. Plaza and T.F. Garetto and J.M. Parera, React. Kinet. Catal. Lett. **20** 1-6 (1982).
- [41] C.R. Apesteguia and J.F. Plaza and T.F. Garetto and J.M. Parera, Applied Catalysis **4** 5-11 (1982).
- [42] T.L. Slager and C.H. Amberg, Can. J. of Chemistry **5** 379 (1991).
- [43] E. Wallin, J.M. Andersson, E.P. Münger, V. Chirita, U. Helmersson, Phys. Rev. B **74** 125409 (2006).
- [44] P.D. Tepesch, A.A. Quong, Phys. Status Solidi B **217** 377 (2000).
- [45] Z. Lodziana, J.K. Norskov, J. Chem. Phys. **115** 11261 (2001).

# Acta Universitatis Upsaliensis

*Digital Comprehensive Summaries of Uppsala Dissertations  
from the Faculty of Science and Technology 871*

Editor: The Dean of the Faculty of Science and Technology

A doctoral dissertation from the Faculty of Science and Technology, Uppsala University, is usually a summary of a number of papers. A few copies of the complete dissertation are kept at major Swedish research libraries, while the summary alone is distributed internationally through the series Digital Comprehensive Summaries of Uppsala Dissertations from the Faculty of Science and Technology.



ACTA  
UNIVERSITATIS  
UPSALIENSIS  
UPPSALA  
2011

Distribution: [publications.uu.se](http://publications.uu.se)  
urn:nbn:se:uu:diva-160270